

Geochemistry, Geophysics, Geosystems®

RESEARCH ARTICLE

10.1029/2022GC010775

Special Section:

Africa plate geosystems

Key Points:

- New seismic data from the Turkana Depression enhances images of East African mantle wavespeed and discontinuity structure
- Thinnest transition zone in East Africa is below the NW Turkana Depression and is underlain by a mid to lower mantle plume tail
- Refractory lithosphere in SE Ethiopia governed northern extent of Mesozoic Anza rifting and southeastern limit of flood basaltic magmatism

Supporting Information:

Supporting Information may be found in the online version of this article.

Correspondence to:

A. Boyce,
alistair.boyce@univ-lyon1.fr

Citation:

Boyce, A., Kounoudis, R., Bastow, I. D., Cottaar, S., Ebinger, C. J., & Ogden, C. S. (2023). Mantle wavespeed and discontinuity structure below East Africa: Implications for Cenozoic hotspot tectonism and the development of the Turkana Depression. *Geochemistry, Geophysics, Geosystems*, 24, e2022GC010775. <https://doi.org/10.1029/2022GC010775>

Received 18 NOV 2022

Accepted 15 JUN 2023

Author Contributions:

Conceptualization: A. Boyce, I. D. Bastow

Data curation: A. Boyce, R. Kounoudis, I. D. Bastow, S. Cottaar, C. J. Ebinger, C. S. Ogden

© 2023 The Authors. *Geochemistry, Geophysics, Geosystems* published by Wiley Periodicals LLC on behalf of American Geophysical Union. This is an open access article under the terms of the [Creative Commons Attribution License](#), which permits use, distribution and reproduction in any medium, provided the original work is properly cited.

Mantle Wavespeed and Discontinuity Structure Below East Africa: Implications for Cenozoic Hotspot Tectonism and the Development of the Turkana Depression



A. Boyce^{1,2} , R. Kounoudis³ , I. D. Bastow³ , S. Cottaar¹ , C. J. Ebinger⁴ , and C. S. Ogden^{3,5} 

¹Department of Earth Science, Bullard Laboratories, University of Cambridge, Cambridge, UK, ²Université Claude Bernard Lyon 1, ENS de Lyon, CNRS, UMR 5276 LGL-TPE, Villeurbanne, France, ³Department of Earth Science and Engineering, Royal School of Mines, Imperial College London, London, UK, ⁴Department of Earth and Environmental Sciences, Tulane University, New Orleans, LA, USA, ⁵School of Geography and Geology, University of Leicester, Leicester, UK

Abstract Ethiopia's Cenozoic flood basalt magmatism, uplift, and rifting have been attributed to one or more mantle plumes. The Nubian plate, however, has drifted 500–1,000 km north since initial magmatism at ~45 Ma, having developed above mantle that now underlies the northern Tanzania craton and the low-lying Turkana Depression. Unfortunately, our knowledge of mantle wavespeed structure and mantle transition zone (MTZ) topography below these regions is poorest, due to a historical lack of seismograph stations. The same data gap means we lack constraints on lithospheric structure in and around the NW–SE trending Mesozoic Anza rift. We exploit data from new seismograph networks in the Turkana Depression and neighboring northern Uganda to develop AFRP22, a new African absolute P-wavespeed tomographic model that resolves whole mantle structure along the entire East African rift system. We also map MTZ thickness using Ps receiver functions. East Africa's thinnest MTZ (~25 km thinning) underlies the northwest Turkana Depression. AFRP22 reveals a co-located, previously unrecognized, slow wavespeed plume tail, extending from the MTZ, deep into the lower mantle. This plume may thus have contributed, along with the African Superplume, to the development of the 45–30 Ma flood basalt province that preceded extension. Pervasive sub-lithospheric slow wavespeeds imply that Turkana's present-day low elevation is explained best by Mesozoic and Cenozoic-age crustal thinning. At ~100 km depth, AFRP22 illuminates a fast wavespeed SE Ethiopian plateau. In addition to governing the northernmost limit of Mesozoic Anza rifting, the refractory nature of this lithospheric block likely minimized Cenozoic flood basalt magmatism there.

Plain Language Summary The Ethiopia-Yemen plateau is capped by Earth's youngest continental flood basalt province. Its development, and that of the East African Rift that bisects it, has been linked to the presence of one or more mantle plumes. However, the African plate has moved 500–1,000 km north since the initial flood basalt phase at ~45 Ma, meaning the mantle that underlies it is now overlain by northernmost Uganda and the low-lying Turkana Depression. The Depression separates the Ethiopia-Yemen and East African plateaus and was once the site of failed NE–SW rifting in Mesozoic time (S. Sudan and Anza rifts). Here, we use two complementary techniques to image the mantle beneath East Africa using new recordings of distant earthquakes collected in the Turkana Depression and northernmost Uganda alongside existing data from across Africa. Combined, these methods help illuminate where hot mantle rock has risen to the surface within mantle plumes and resulted in magmatism. Intriguingly, East Africa's hottest mantle today, at transition zone depths, underlays the Ethiopian flood basalt province at 30 Ma. At shallower depths, a fast seismic wavespeed zone in SE Ethiopia, which was unaffected by flood basaltic magmatism, likely controlled the location of earlier episodes of failed Anza rifting.

1. Introduction

1.1. Overview

The uplifted Ethiopia-Yemen plateau is home to the world's youngest continental flood basalt province (Figure 1). The East African plateau lies to the south, but continuous high elevation in East Africa is broken by the low-lying, ~300–500 km wide Turkana Depression of southernmost Ethiopia/northern Kenya. Cenozoic development of uplifted plateaus, along with that of the East African Rift (EAR) system that bisect them, has long been linked to a plume-affected mantle (e.g., Ebinger & Sleep, 1998; George et al., 1998; Ritsema

Formal analysis: A. Boyce, R. Kounoudis, C. S. Ogden

Funding acquisition: I. D. Bastow, S. Cottaar, C. J. Ebinger

Investigation: A. Boyce, R. Kounoudis, C. S. Ogden

Methodology: A. Boyce

Project Administration: A. Boyce, I. D. Bastow, S. Cottaar, C. J. Ebinger

Resources: I. D. Bastow, S. Cottaar

Software: A. Boyce

Supervision: I. D. Bastow, S. Cottaar

Validation: A. Boyce

Visualization: A. Boyce

Writing – original draft: A. Boyce, R. Kounoudis, C. S. Ogden

Writing – review & editing: A. Boyce, R. Kounoudis, I. D. Bastow, S. Cottaar, C. J. Ebinger, C. S. Ogden

et al., 1998; Rogers et al., 2000). However, consensus on the number of mantle plumes that underlie East Africa, as well as their morphology and depth extent, is lacking (e.g., Boyce et al., 2021; Chang & van der Lee, 2011; Civiero et al., 2015; Emry et al., 2019; Pik et al., 2008; Tsekhmistrenko et al., 2021). Of particular importance in our understanding of Ethiopia's hotspot tectonism is present-day seismic structure below the 300–500 km-wide Turkana Depression of southernmost Ethiopia and northernmost Kenya (Figure 1). The Ethiopia-Yemen Highlands overlay these regions 30 Ma ago, before Africa drifted ~500–1,000 km north to its present day position (e.g., Müller et al., 2018). Unfortunately, a historical paucity of seismograph stations has rendered it impossible to confidently resolve whole mantle wavespeed and mantle transition zone topography below this critical region, meaning plume-flood basalt province correlations are difficult to substantiate. The Turkana Depression itself represents a geodynamical puzzle too: specifically whether it owes its low-lying nature (~500 m) to crustal thinning (e.g., Benoit, Nyblade, & Pasyanos, 2006; Ogden et al., 2023), or a lack of mantle dynamic support (e.g., Rogers et al., 2000). The extent to which the location of the failed, NW–SE-trending Mesozoic-age Anza rift was influenced by lithospheric heterogeneity and its connection to the Central African rift system in Sudan are also poorly constrained.

Utilizing broadband seismic data recorded by two recent temporary seismograph networks in the Turkana Depression and neighboring northern Uganda, we develop a new African absolute P-wavespeed tomographic model (AFRP22), and a P-to-s receiver function study of the mantle transition zone, providing the first such constraints between East Africa's two uplifted plateaus. The presence of warm upwelling material typically results in slow seismic wavespeeds and a thinned mantle transition zone (MTZ) due to the opposing Clapeyron slopes of the d410 and d660 phase transitions (e.g., Helffrich, 2000). In tandem, these methods allow us to explore the thermochemical state of the mantle both in present-day and 30 Ma plate configurations. At uppermost mantle depths our tomographic models allow us to distinguish slow-wave speed zones associated with present-day rifting, from fast wave speed lithospheric structures that have resisted thermomechanical erosion.

1.2. Tectonic Setting

The Cenozoic EAR extends from Afar to southern Africa, traversing the elevated Ethiopia-Yemen (~2.5 km) and East African plateaus (~1.5 km) as well as seafloor east of the continent (Figure 1). The low-lying, 300–500 km-wide, Turkana Depression separates the two plateaus, where the Main Ethiopian Rift and Eastern Rift branches of the EAR meet. The Depression has hosted multiple, superposed phases of rifting: during the Cretaceous (130–80 Ma), Paleogene (66–50 Ma) and Miocene–recent (25–0 Ma; Ebinger et al., 2000; Morley et al., 1992). The first two phases constituted the failed NW–SE-trending Anza and S. Sudan rifts (Macgregor, 2015; Purcell, 2018), which are now traversed orthogonally by the N–S-trending EAR (Figure 1).

East Africa's pre-Cenozoic rift lithosphere comprised numerous Archean cores (e.g., the Tanzania craton; Figure 1) that sutured along Proterozoic-age mobile belts during the East African Orogen (700–550 Ma; Fritz et al., 2013). Subsequent rifting has generally localized to these mobile belts, though preserved remnants of island-arc terranes and/or stacked microcontinents within them have also influenced the development of Mesozoic and Cenozoic rifting (e.g., Kounoudis et al., 2021). Below southeasternmost Ethiopia, the reason for the lack of rifting and magmatism, is uncertain.

The main phase of Cenozoic magmatism and uplift in East Africa is often attributed to the presence of one or more mantle plumes (e.g., Ebinger & Sleep, 1998; George et al., 1998; Nelson et al., 2012; Pik et al., 2003; Rooney, 2017). Ebinger and Sleep (1998) suggest that plume material impinged on East African lithosphere below the Turkana Depression ca. 45 Ma, concurrent with earliest East African magmatism (Furman et al., 2006; George et al., 1998). Although the Turkana Depression is low-lying in comparison to the elevated plateaus, it too has experienced 0.6 km of uplift since the Neogene, prior to which it was close to sea-level (Brown & McDougall, 2011). The Turkana Depression's significantly thinned crust (e.g., Benoit, Nyblade, & Pasyanos, 2006; Ogden et al., 2023) allows the possibility that the elevated East African and Ethiopia-Yemen plateaus are part of a single geodynamic setting, all underlain by buoyant plume-influenced mantle.

1.3. Previous Mantle Tomography and Transition Zone Receiver Function Studies

A common feature in global tomographic studies is a broad, slow wavespeed zone originating at the core-mantle boundary (CMB) beneath southern Africa, often termed the African Superplume (e.g., Li et al., 2008; Ritsema

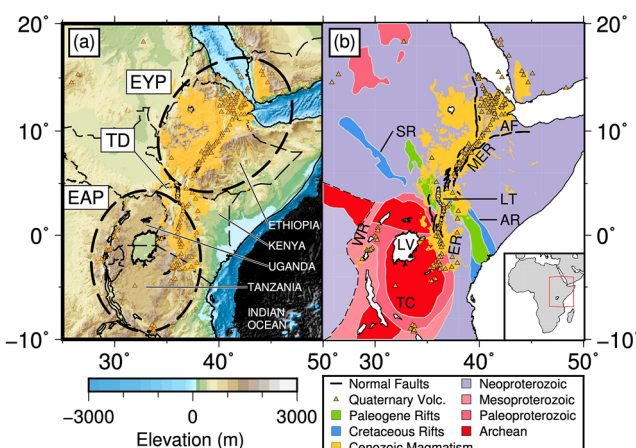


Figure 1. (a) Elevation in East Africa. The Ethiopia-Yemen (EYP) and East African (EAP) topographic plateaus are separated by the Turkana Depression (TD). Dashed black lines: National boundaries. (b) Broad-scale East African tectonics modified after Begg et al. (2009) and Kounoudis et al. (2021). Inset: Study region within Africa. AF: Afar Depression, AR: Anza Rift, ER: Eastern Rift, LT: Lake Turkana, LV: Lake Victoria, MER: Main Ethiopian rift, SR: South Sudan Rift, TC: Tanzanian Craton, WR: Western Rift.

et al., 1999). Numerous authors (e.g., Civiero et al., 2015, 2019; Emry et al., 2019; Montagner et al., 2007) suggest the African Superplume splits into several, laterally distinct, slow wavespeed plume stems in the upper mantle along the EAR. Others have hypothesized that two or three distinct plume heads (e.g., Chang & van der Lee, 2011; Chang et al., 2020; Pik et al., 2008; Tsekhnistrenko et al., 2021), and/or two distinct deep-seated mantle plumes may underlie the region (Boyce et al., 2021; Montelli et al., 2006).

Continent-scale ambient noise (Emry et al., 2019), surface-wave (Celli et al., 2020; Civiero et al., 2022), body-wave (Boyce et al., 2021; Hansen et al., 2012) tomography, and their joint inversion (Chang & van der Lee, 2011), image the Turkana Depression as a broad anomalously slow wavespeed zone. However, these tomographic studies lack seismograph station coverage within the Depression itself. Similarly, while RF studies of the East African mantle reveal a thinner mantle transition zone below southern Ethiopia, than below the Main Ethiopian Rift to the north and the Eastern and Western Rifts to the south (e.g., Benoit, Nyblade, Owens, & Stuart, 2006; Boyce & Cottaar, 2021; Cornwell et al., 2011; Mulibio & Nyblade, 2013; Nyblade et al., 2000; Owens et al., 2000; Reed et al., 2016; Sun et al., 2017; Thompson et al., 2015), transition zone structure below the Turkana Depression remains unconstrained. Recent work has however investigated the presence of upper mantle discontinuities here (Pugh et al., 2023).

Kounoudis et al. (2021) used data spanning the period January 2019 to September 2020 from the recently deployed Turkana Rift Arrays Investigating Lithospheric Structure (TRAILS) seismic network to construct a relative arrival-time tomographic model centered on the Turkana Depression. Their images show low wavespeeds throughout the Turkana Depression's upper mantle, implying there is no evidence for a break in dynamic support between the uplifted Ethiopia-Yemen and East African plateaus. Instead, crustal RF analysis (Ogden et al., 2023) shows a 20–30 km-deep Moho below the TRAILS network, implying that the region's low elevations can be explained adequately by crustal thinning alone. Shallower than 150 km depth, Kounoudis et al. (2021) illuminate a narrow (~50 km-wide), NW–SE-trending, fast wavespeed band, interpreted as Proterozoic-age refractory lithosphere, sitting atop a diffuse low wavespeed anomaly. However, their study lacked broadband seismograph station coverage in northern Uganda and on the SE Ethiopian plateau. Further, their use of relative, not absolute arrival-time data, precludes the possibility of direct comparison of anomaly amplitudes with terranes to the north and south of the Turkana Depression, due to removal of the background mean in the calculation of relative arrival-times (e.g., Bastow, 2012).

ing Lithospheric Structure (TRAILS) seismic network to construct a relative arrival-time tomographic model centered on the Turkana Depression. Their images show low wavespeeds throughout the Turkana Depression's upper mantle, implying there is no evidence for a break in dynamic support between the uplifted Ethiopia-Yemen and East African plateaus. Instead, crustal RF analysis (Ogden et al., 2023) shows a 20–30 km-deep Moho below the TRAILS network, implying that the region's low elevations can be explained adequately by crustal thinning alone. Shallower than 150 km depth, Kounoudis et al. (2021) illuminate a narrow (~50 km-wide), NW–SE-trending, fast wavespeed band, interpreted as Proterozoic-age refractory lithosphere, sitting atop a diffuse low wavespeed anomaly. However, their study lacked broadband seismograph station coverage in northern Uganda and on the SE Ethiopian plateau. Further, their use of relative, not absolute arrival-time data, precludes the possibility of direct comparison of anomaly amplitudes with terranes to the north and south of the Turkana Depression, due to removal of the background mean in the calculation of relative arrival-times (e.g., Bastow, 2012).

2. Body-Wave Mantle Seismic Tomography

2.1. New Absolute Arrival-Time Data

New broadband seismic data come from permanent GEOFON station LODK in Kenya, and recent temporary networks in the Turkana Depression (Bastow, 2019; Ebinger, 2018; Kounoudis et al., 2021), northern Uganda, (Andriampomenana et al., 2021; Nyblade, 2017), Mozambique (Fonseca et al., 2014; Helffrich & Fonseca, 2011) and Namibia (Durrheim & Nyblade, 2009; Nyblade, 2015). Following the Absolute Arrival-time Recovery Method (AARM; Boyce et al., 2017), we align waveforms following VanDecar and Crosson (1990) to form a high signal-to-noise ratio stack, on which first arrival-times are picked manually. This process yields 13,455 direct and 1299 core P-wave absolute arrival-times (Figure 2a) for use in subsequent global-scale tomographic inversion. Earthquake, station, and mean P-wave absolute arrival-time residual distributions are shown in Figures S1–S3 and S4–S12 in Supporting Information S1 show additional details of the procedure used to determine arrival-times for each temporary network.

Prior to tomographic inversion, absolute arrival-times are corrected for station elevation and Earth's ellipticity (following Kennett & Gudmundsson, 1996). We also apply a crustal (Moho depth) correction using Crust1.0 (Laske et al., 2013), supplemented wherever possible by RF and wide-angle seismic constraints (Figures S13 and S14 in Supporting Information S1). To the earlier crustal model compiled by Boyce et al. (2021), we add data

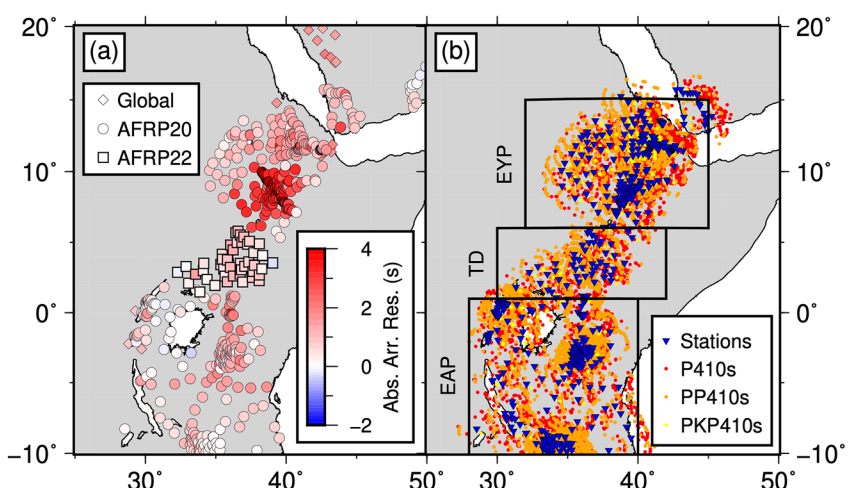


Figure 2. (a) Mean absolute arrival-time residuals, corrected for Earth ellipticity and station elevation, throughout East Africa. Negative residuals indicate early arrivals; positive residuals indicate late arrivals with respect to ak135 (Kennett et al., 1995). (b) Receiver function P410s/PP410s/PKP410s piercing points.

from numerous authors (Braile et al., 1994; Heit et al., 2015; Mechie et al., 1994; Ogden et al., 2023; Prodehl et al., 1994). Correcting a sign error in the implementation of the topographic and ellipticity travel-time corrections in Boyce et al. (2021) renders delay times slightly earlier in this study, but also improves imaging of shallow mantle features beneath East Africa. Specifically, an decrease in the mean of 87,184 recalculated arrival-times from Boyce et al. (2021) by 1.3 s, yields a minor increase in the average wavespeed anomaly of the resulting tomographic model by 0.087%, with respect to ak135.

2.2. Absolute P-Wavespeed Tomographic Inversion

We use the “EHB” global data set of mantle and core phases recorded from 1964 to 2004 (Engdahl et al., 1998), to constrain the background Earth model, alongside the AARM-derived data set described in Section 2.1. We follow the absolute P-wavespeed tomographic inversion approach of Li et al. (2008) and Boyce et al. (2021). Initially, rays traced through the 1D reference model ak135 are clustered into composite rays according to station and earthquake proximity. Composite rays are weighted by the square root of the number of rays within each cluster (Káráson & Van der Hilst, 2001). Cells within the initial regularly parameterized global grid (45 km in depth, 0.35° in latitude and longitude), are combined with adjacent cells to obtain a minimum sampling of 900 rays per cell (Figure S15 in Supporting Information S1). We solve for hypocenter mislocation and slowness perturbations with respect to ak135 on the adaptively parameterized grid using an iterative, linearized, least squares inversion approach to minimize the cost function:

$$\epsilon = w\|Gm - d\|^2 + \lambda_1\|Lm\|^2 + \lambda_2\|m\|^2. \quad (1)$$

Comparison between the sensitivity matrix G , model, m , and data d , is weighted by w in the first term. In line with Boyce et al. (2021), we impose a weighting three times greater for the AARM derived African data sets compared to the EHB global data set (e.g., Káráson & Van der Hilst, 2001; Li et al., 2008). Regularization is applied through smoothing in the second term, using the first derivative smoothing operator in horizontal and vertical directions, L , and damping by the model norm in the third term. Weights associated with these terms are applied by λ_p chosen via trade-off analysis. We independently vary the horizontal gradient smoothing and the vertical gradient smoothing, prior to varying both together, to select an appropriate model close to the “knee” of the combined trade-off curve (Figure S16 in Supporting Information S1). Although our model is global in scope, we focus our attention primarily on East Africa where significant resolution gains have been made over previous studies (e.g., Boyce et al., 2021; Celli et al., 2020; Hansen et al., 2012).

2.3. Tomographic Resolution Assessment

We test the resolution of realistic upper mantle structures, various plume configurations and checkerboard anomalies (Figure 3; Figures S17–S31 in Supporting Information S1). We invert synthetic arrival-time data, calculated

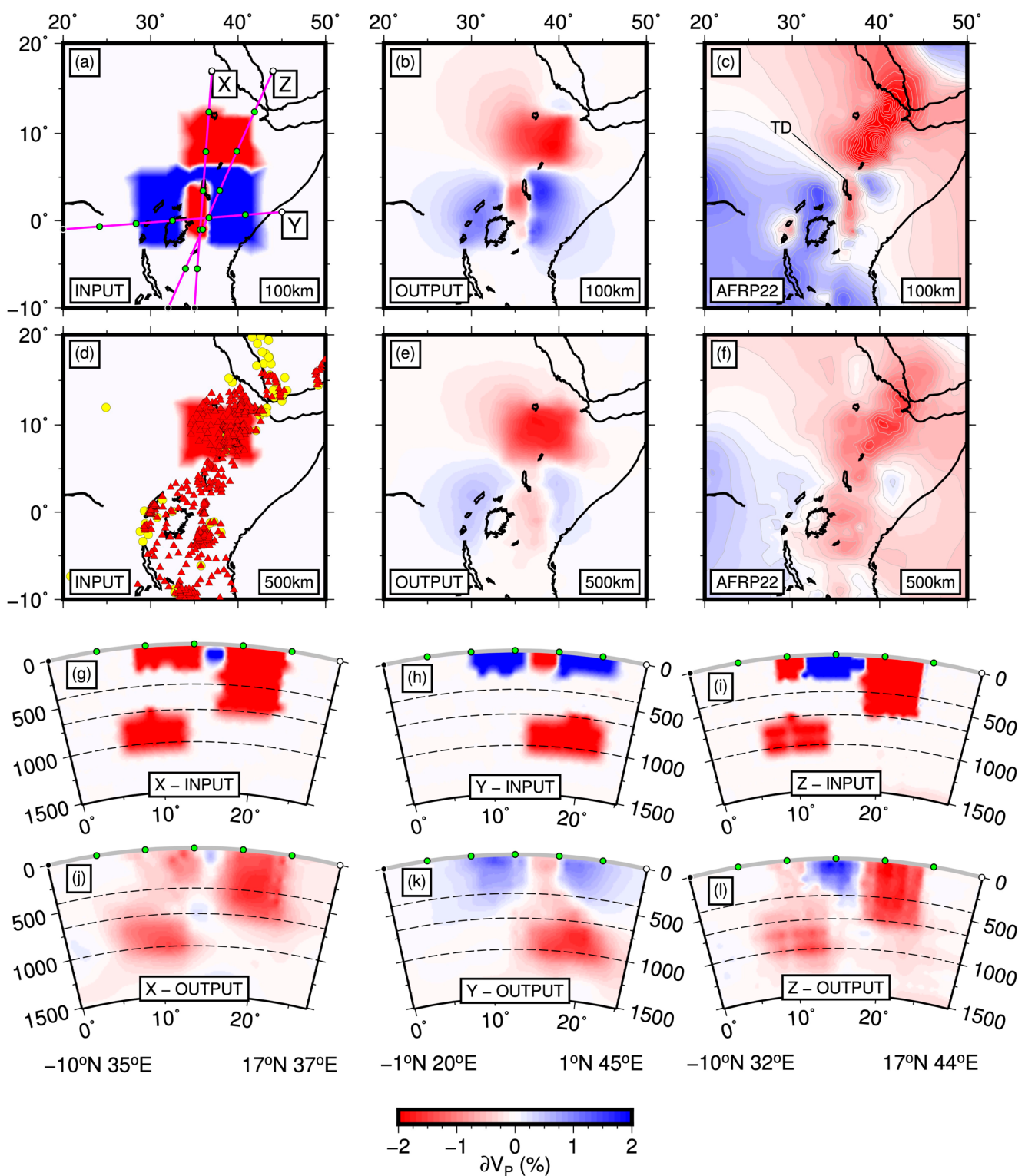


Figure 3. Structural resolution test of variable wavespeed structure in the upper mantle (a, d, and g–i) compared to AFRP22 (c, f). Input anomaly amplitudes are $\delta V_p = \pm 2.0\%$. The input narrow north-south slow wavespeed anomaly below the Turkana Depression is 3° wide in longitude and extends to 250 km depth. Meanwhile, to the north, the narrow east-west fast wavespeed band is 2° wide in latitude and extends to 150 km depth. Yellow circles: “EHB” stations; red triangles: seismograph stations analyzed here. Visual defects within input models arise from coarse adaptive parameterization due to poor ray path sampling. Other labels as in previous figures.

using identical ray paths to observed data, including 0.2 s standard deviation Gaussian noise. Figure 3 indicates good horizontal and vertical resolution of upper mantle slow wavespeeds below the Ethiopia-Yemen plateau. The narrow, N-S-oriented slow wavespeed anomaly (3° width) in northern Kenya, is well recovered spatially, but with reduced amplitudes, especially toward the south. The edges of adjacent fast velocity features are smeared laterally. Our model cannot recover a narrow (2° width) fast wavespeed band at 100 km depth in southernmost Ethiopia, not dissimilar to that seen by Kounoudis et al. (2021, see Section 1.3). Shallow mantle slow wavespeeds below the Turkana Depression and northern Kenya are smeared vertically and so cannot be clearly separated in depth from an anomaly below the MTZ. Slow wavespeeds below the MTZ are reasonably well constrained laterally however (Figures 3j and 3l).

Further resolution tests for one, two and three isolated slow wavespeed anomalies below the Ethiopia-Yemen plateau, the East African plateau and the Turkana Depression, over a range of depth extents are documented in Figures S17–S20 in Supporting Information S1. Lateral smearing is relatively minor between anomalies in the upper mantle, but increases toward 1,000 km depth. Below the transition zone, vertical smearing of a few hundred kilometers occurs. A slow wavespeed anomaly below the Turkana Depression extending to the CMB, can be resolved by AFRP22 (Figure S20 in Supporting Information S1) but with reduced amplitudes below 1,500 km depth. Narrow ($\sim 2\text{--}3^\circ$ width), upper mantle slow wavespeed anomalies are partially resolvable below dense station coverage (Figure S21 in Supporting Information S1). Figure S22 in Supporting Information S1 shows the resolution of cratons and two whole mantle plumes. The broad ($14^\circ\text{--}28^\circ$ wide), inclined slow wavespeed anomaly extending to the lower mantle below southern Africa is reasonably well recovered throughout the entire mantle (recovery amplitude $>60\%$). The narrow ($5^\circ\text{--}10^\circ$ wide), vertical slow wavespeed anomaly below Ethiopia is well recovered above $\sim 1,500$ km depth but drops to $\sim 30\%$ recovery amplitude at the base of the mantle. Lateral smearing of these two slow wavespeed anomalies increases with depth, especially below 1,500 km. Figure S23 in Supporting Information S1 shows the recovery of a slow wavespeed, broad mid-to-lower mantle anomaly representing ponded material. Figures S24–S25 in Supporting Information S1 shows connectivity of upper and lower mantle anomalies may be uncertain when an amplitude reduction of $\sim 1/3$, compared to that above and below, occurs over a 300–700 km depth interval. These tests can be compared to previous work (Boyce et al., 2021). Resolution is mainly improved in the upper-mid mantle beneath the Turkana Depression. Traditional checkerboard tests with anomalies for $2^\circ\text{--}10^\circ$ are presented in Figures S26–S31 in Supporting Information S1. We conclude that in East Africa, in regions of sufficient station coverage, reliable recovery of ~ 300 km width anomalies can be expected at shallow mantle depths with $>50\%$ amplitude. Anomalies of $\sim 500\text{--}1,000$ km width are better recovered below the MTZ in eastern and southern Africa.

2.4. Tomographic Results

Figures 4–6 show AFRP22 at a variety of scales. At 100 km depth, slow wavespeed anomalies ($\delta V_p \approx -0.9\%$) underlie the Turkana Depression but drop in amplitude northwards into southern Ethiopia ($\delta V_p \approx -0.3\%$). The highest amplitude slow wavespeed anomalies at 100 km depth ($\delta V_p \approx -3.0\%$) are below the NW Ethiopian plateau, the Main Ethiopian Rift, and Afar (Figures 4 and 6). At 100 km depth, AFRP22 also resolves fast wavespeed structure ($\delta V_p \approx 0.8\%$) below the southeasternmost Ethiopian plateau. South of the Turkana Depression, low wavespeed structure underlies Quaternary volcanoes at 100 km depth along the eastern and western rifts (Figures 4 and 6). At ≥ 200 km depth, slow wavespeed anomalies are relatively constant below the Ethiopia-Yemen flood basalt province and more recent Quaternary volcanism associated with the Main Ethiopian Rift, Eastern Rift, and Afar ($\delta V_p \leq -0.5\%$). Fast wavespeed structure ($\delta V_p \geq +1.0\%$) is also recovered below the Tanzania craton (Figure 4), akin to other Archean cores across Africa (Figure 5a). However, the Tanzanian fast wavespeed anomaly reduces in amplitude to $\delta V_p \leq +0.7\%$ at greater lithospheric depths (>100 km, e.g., Figures S32 and S35 in Supporting Information S1). Resolution tests show the observations above are robust (e.g., Figure 3; Figures S17–S31 in Supporting Information S1). However, we cannot preclude the possibility that Tanzanian craton fast wavespeeds are affected by both vertical smearing and/or some overprinting from underlying slow wavespeeds (e.g., Figure 3; Figure S22 in Supporting Information S1).

In the upper MTZ (410 km depth), slow wavespeeds ($\delta V_p \geq -0.8\%$) persist continuously from Afar to the southernmost Eastern Rift (Figure 4); anomalies below the Western Rift are comparatively low amplitude ($0.15\% > \delta V_p > -0.15\%$). In the lower MTZ (660 km depth), at least two distinct slow wavespeed anomalies emerge (A, B, $\delta V_p \leq -1.0\%$; Figure 4), below the Ethiopia-Yemen and East African plateaus, respectively. Anomaly amplitudes below the eastern Turkana Depression are lower ($\delta V_p \geq -0.5\%$).

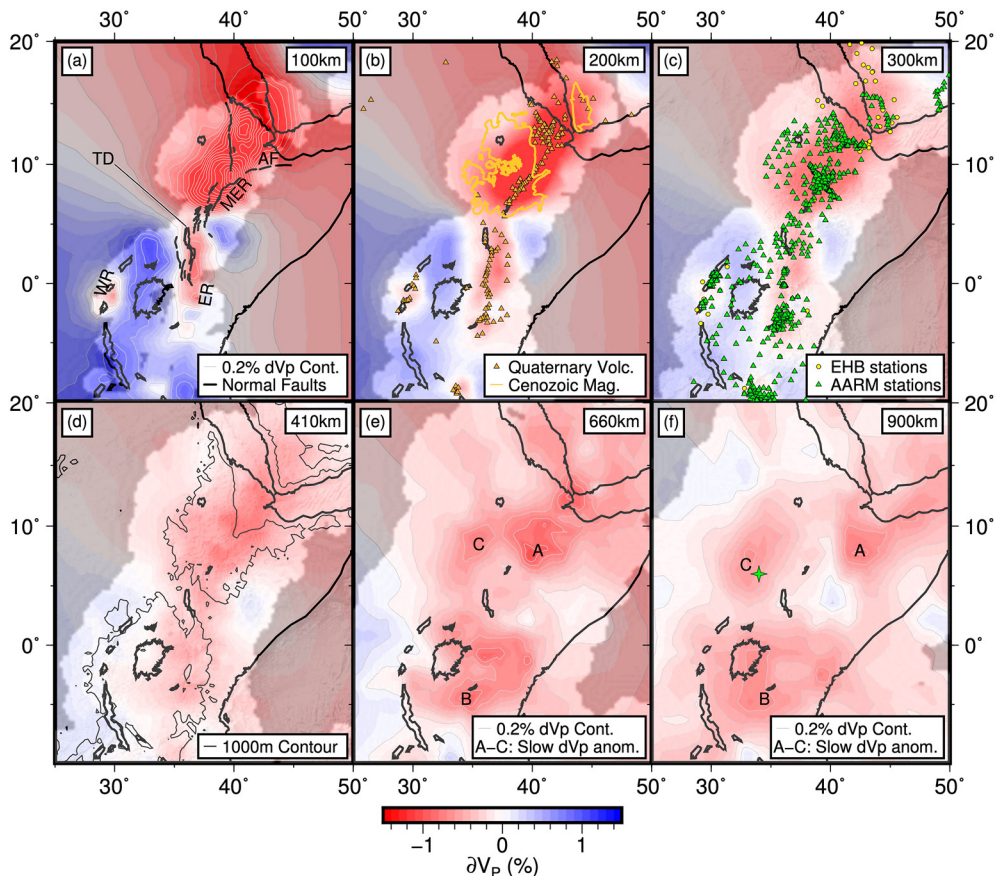


Figure 4. AFRP22 African tomographic depth slices at 100–900 km depth, focused on East Africa, plotted as percentage deviation from ak135. Only the global data set constrains the gray regions, according to the projected ray paths of our seismograph station data (See Supporting Information S1). Panels (a–c) slow wavespeed anomalies discussed in the main text. Green star in f: plume location proposed by Vicente de Gouveia et al. (2018), distinct from any present-day upwellings below Ethiopia-Yemen or East African plateaus. Other labels as in previous figures.

Additionally, a third slow wavespeed anomaly emerges in southwest Ethiopia at and below 660 km depth (anomaly C, $\delta V_p \approx -0.4\%$, Figures 4 and 5; Figures S33–S39 in Supporting Information S1), and remains isolated from anomalies A and B, as it persists vertically into the lower mantle (>2,300 km depth). In the lower mantle, anomaly B persists to the south-southwest below southern Africa. Anomaly A persists to the east below the Indian Ocean, bifurcating at ~1,600 km depth (Figure 5e). No clear amplitude reduction, compared to anomalies above and below, are seen within anomalies A, B or C (Figure 5; Figure S35 in Supporting Information S1) to render a connection between upper- and lower-mantle anomalies significantly uncertain (Figures S24–S25 in Supporting Information S1). AFRP22 is visualized in 3D renderings, and compared to previous models (e.g., Hosseini et al., 2019; Li et al., 2008; Montelli et al., 2006; Simmons et al., 2012), in the Supporting Information S1 Figures S36–S40 in Supporting Information S1.

3. P-to-s Mantle Transition Zone Receiver Functions

3.1. Receiver Function Data

We constrain MTZ discontinuity structure by calculating P-to-s RFs to isolate P410s and P660s converted phases, arriving across East Africa. Our data processing procedure uses SMURFPy (Cottaar et al., 2020) and follows Boyce and Cottaar (2021), whose data set of >28,400 RFs we supplement with newly available data, as per Section 2.1. We calculate P-to-s RFs from P, PP, and PKP phases using minimum magnitudes of $5.0 M_w$, $6.2 M_w$ and $6.2 M_w$ and limit our epicentral distance ranges to 40° – 90° , 100° – 125° and 145° – 150° respectively, to prevent interference with other phases (Figures S41–S43 in Supporting Information S1). Our new data set comprises 467

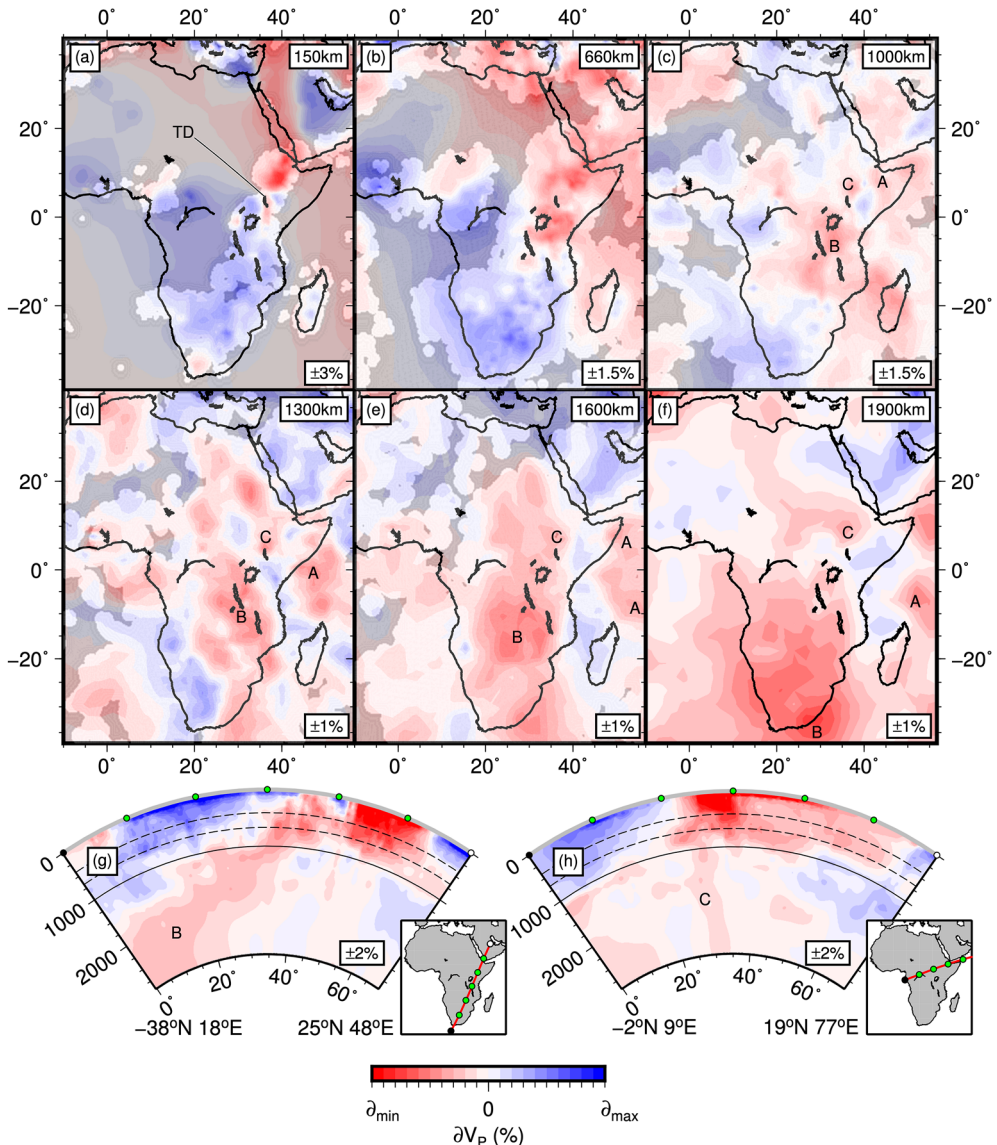


Figure 5. AFRP22 African tomographic model shown at the continent-scale from upper-to-lower mantle depths in map (a–f) and cross-section (g–h). All figures plotted as percentage deviation from ak135 shown in lower right. Only the global data set constrains the gray regions (See Supporting Information S1). Features A–C are discussed in the main text. Other labels as in previous figures.

Pds RFs, 421 PPds RFs and 23 PKPds RFs from East African stations and a further 611 RFs from stations in Mozambique and Namibia. d410 piercing points for the African data set are shown in Figure 2b and Figure S44 in Supporting Information S1. We window raw data from 25 s before, to 150 s after the direct-P wave, and filter from 0.01 to 0.2 Hz. We calculate RFs using time domain iterative deconvolution (Ligorria & Ammon, 1999), with a Gaussian pulse of 5 s or 0.2 Hz maximum width. Higher maximum frequencies, ≤ 0.9 Hz, are also tested and subject to identical quality control. The precise quality control steps are given by Boyce and Cottaar (2021).

3.2. Stacking Techniques

We use epicentral distance (Figures S41–S43 in Supporting Information S1), depth and slowness (Figures S45–S46 in Supporting Information S1) stacks to assess the validity of our results at continental and regional scales. Depth stacks are constructed using RFs migrated to depth using both AF2019 (Celli et al., 2020) and AFRP22 (Section 2). To reconstruct MTZ discontinuity structure in 3D, we use common conversion point stacking (CCP;

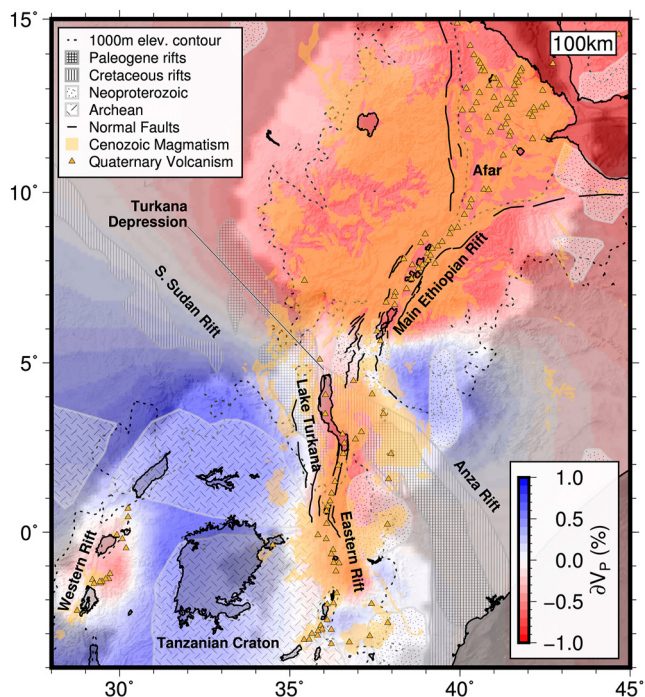


Figure 6. AFRP22 tomographic model in East Africa at 100 km depth plotted as percentage deviation from ak135. Only the global data set constrains the gray regions (See Supporting Information S1). Precambrian crustal domains are after Begg et al. (2009) and Kounoudis et al. (2021).

in space as we will impose here. Notably, the presence of variable quantities of melt in East Africa may impact the relationship between δV_s and δV_p , because of greater S-wavespeed sensitivity to melt than P-wavespeed (e.g., Hammond & Humphreys, 2000). For example, based on analysis of P- and S-wave relative arrival-time residuals, Bastow et al. (2005) suggest the presence of shallow, localized melt below the Main Ethiopian Rift. Meanwhile Civiero et al. (2016) and Kounoudis et al. (2021) find comparably less melt in the surrounding regions of Ethiopia and further south below the Turkana Depression.

Boyce and Cottaar (2021) assumed the relationship $\delta V_s = \delta V_p \times (\text{depth}/2891 + 2)$, following Ritsema et al. (2011), which in practice means a conversion factor close to 2 for the upper mantle. Here, we quantitatively explore the results for factors of 2–3. The most favorable parameter/velocity model will minimize the correlation between d410 and d660 depths across the CCP stacks, and minimize the magnitude difference between the correlation of discontinuity depths and the topographic correction on those depths (van Stiphout et al., 2019). This approach assumes an olivine dominated mantle. Locally, correlations could differ due to the presence of garnet. Results using the AFRP22 P-wavespeed model and the AF2019 S-wavespeed model are shown in Figures S49 and S50 in Supporting Information S1. None of the scaling factors result in an anti-correlation between d410 and d600. For AFRP22, best results are achieved when the upper mantle scaling constraint from δV_p to δV_s is 2.7. Testing of AF2019 shows little improvement by varying this scaling factor, due to the time-to-depth conversions being more sensitive to stronger shear wavespeed variations.

We proceed with the scaling relationship used by Boyce and Cottaar (2021) for S-wavespeed models but use our improved scaling relationship with a factor of 2.7 at the surface for AFRP22. With these choices, the strongest shear wave anomaly of -9.5% in the converted AFRP22 model compares to the value of -9.3% in AF2019. However, neither model captures the slowest S-wavespeeds in Africa of $\delta V_s \approx -11\%$ that have been observed along the central and northern Main Ethiopian Rift by Gallacher et al. (2016) and Emry et al. (2019), likely related to the melt rich crust and upper mantle (e.g., Bastow et al., 2010; Kendall et al., 2005; Rooney et al., 2005).

e.g., Dueker & Sheehan, 1997). We update the CCP stacks of Boyce and Cottaar (2021) using identical stacking parameters and include the new RF data. Following Boyce and Cottaar (2021), we test time-to-depth corrections (accounting for elevation and the crust), for five 3D mantle absolute wavespeed models against the 1D radial Earth model ak135 (Figures S47–S48 in Supporting Information S1). We use three global S-wavespeed models (SL2013SV, SEMUCB-WM1 and SGLOBEran: Chang et al., 2015; French & Romanowicz, 2014; Schaeffer & Lebedev, 2013), the African continental S-wavespeed model AF2019 (Celli et al., 2020) and our continental P-wavespeed model AFRP22, described in Section 2. To apply the corrections, we require a scaling factor between S-wavespeed anomalies and P-wavespeed anomalies (or vice-versa for AFRP22). We explore the scaling factor and choice of model in the next section (and Figures S49–S50 in Supporting Information S1). We track summed weights and standard errors to normalize stacked amplitudes and limit our interpretations to regions where summed weights are greater than two and relative amplitudes are greater than two standard error from the mean. Figure S47 in Supporting Information S1 shows CCP grid stacking weights at the d410 and d660. Maximum amplitudes within the depth ranges 370–450 km and 620–700 km are chosen to represent converted phases from MTZ discontinuities (Figures S51–S56 in Supporting Information S1).

3.3. Robustness of Discontinuity Depths

3.3.1. Scaling Between δV_s and δV_p

The relationship between δV_s and δV_p in tomographic models is an area of ongoing research (e.g., Lu et al., 2019; Ritsema & Van Heijst, 2002; Tesoniero et al., 2016), and is not required to be linearly related in depth or invariant

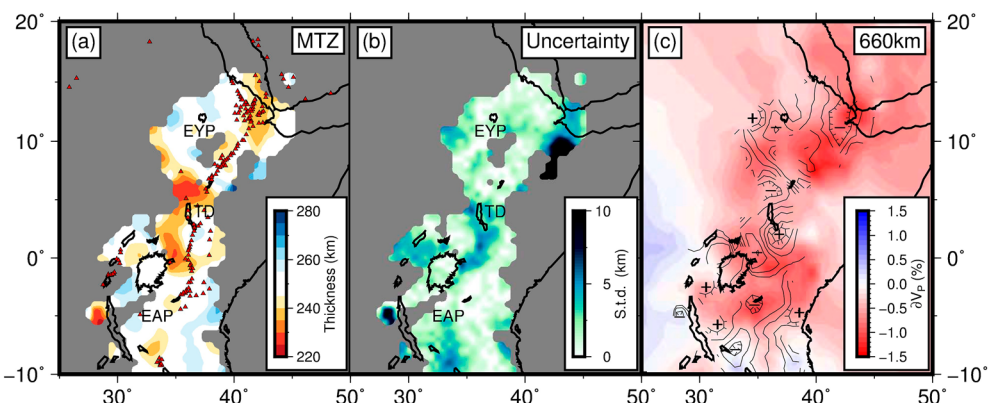


Figure 7. (a) Mean East African MTZ thickness based on AFRP22-CCP and SGLOBEani-CCP. (b) MTZ thickness uncertainty. Only regions in which all CCP stacks provide results are shown. Red triangles: Quaternary volcanism. EYP: Ethiopia-Yemen plateau, EAP: East African plateau, TD: Turkana Depression. (c) 660 km depth slice through AFRP22, plotted as percentage deviation from ak135. Overlain are MTZ thickness contours at 5 km intervals. “Highs” are labeled with a “+”; “lows” are labeled with a “-”. Tick marks indicate “downhill” direction.

3.3.2. Choice of Model

Receiver function CCP stacks are constructed using time-to-depth corrections from the 1D radial Earth model (ak135-CCP), one P-wavespeed tomographic model (AFRP22-CCP) and four S-wavespeed tomographic models (AF2019-CCP, SL2013-CCP, SEMUCB-CCP, SGLOBEani-CCP). For all stacks based on 3D models, the correlation between d410 and d660 topography is suppressed, compared to the stack ak135-CCP. Based on these correlations, all five CCP stacks perform similarly, meaning we cannot base our results on one preferred CCP stack (e.g., Boyce & Cottaar, 2021). However, discontinuity depth results vary between 3D model corrected CCP stacks (see Figures S51–S53 and Tables S2–S5 in Supporting Information S1).

To quantify the variation in 3D model corrected CCP stack results, we take the mean and standard deviations across the five stacks using tomographic models (Figures S54–S56 in Supporting Information S1). Mean uncertainties are ≤ 5.3 km and ≤ 9.7 km across Africa, for d410 and d660 depths respectively. An E-W band of high discontinuity depth uncertainty is present in the Turkana Depression (Figure S54 in Supporting Information S1), but is lacking in MTZ thickness uncertainties (Figure S55 in Supporting Information S1). Detailed interrogation of the tomographic models used for time-to-depth corrections reveals that this high uncertainty region is likely related to resolution differences between tomographic models in the Turkana Depression. AF2019, SL2013 and SEMUCB do not reveal any significant increase in upper mantle wavespeeds in the Depression relative to slow wavespeeds in neighboring Ethiopia and East Africa. Meanwhile, AFRP22 and SGLOBEani reveal some variation between these regions. Consequently, upper mantle wavespeed variations sampled by RFs from the Turkana Depression are mapped into discontinuity depth changes in AF2019-CCP, SL2013-CCP and SEMUCB-CCP, but this effect is substantially less in AFRP22-CCP and SGLOBEani-CCP. We consider that poor resolution of MTZ depth wavespeeds also maps into increased MTZ thickness uncertainties. Better apparent resolution of the Turkana Depression wavespeeds in AFRP22 and SGLOBEani means that while absolute discontinuity depths are uncertain, the relative variations between the Ethiopia-Yemen plateau, the Turkana Depression and the East African plateau may be more consistent in the corresponding CCP stacks. Consequently, we present only MTZ thickness results and favor mean results from AFRP22-CCP and SGLOBEani-CCP (Figure 7a) rather than AF2019-CCP, SL2013-CCP and SEMUCB-CCP, which we consider to be over estimates. Finally, we take a series of conservative precautions (e.g., primary interpretations are based on low frequency stacks: ≤ 0.2 Hz), to limit interpretation of data noise or artifacts following Boyce and Cottaar (2021).

3.4. Receiver Function Results

CCP stacking shows the Turkana Depression hosts a thinned MTZ of $\sim 243 \pm 2.0$ km on average (Figure 7). The strongest thinning, of ≤ 25 km, lies beneath the northwestern Turkana Depression, although uncertainties are relatively elevated here ($s.t.d \approx 5.0$ km). To the north, the Ethiopia-Yemen plateau exhibits a regional MTZ thickness of $\sim 247 \pm 2.0$ km, with average MTZ thickness values in the northwest of ~ 250 km. MTZ thinning

of ≤ 15 km is observed below Afar, and ≤ 10 km below the Main Ethiopian Rift. South of the Turkana Depression, the East African plateau displays a regional MTZ thickness at $\sim 248 \pm 2.0$ km, close to the expected global mean. A small patch of 15–25 km thinning exists northeast of Lake Victoria, in northeast Uganda and western Kenya. The regions with largest uncertainty are eastern Ethiopia and the Western Rift (s.t.d. > 7.5 km, Figure 7b). Elsewhere beneath Africa (Figures S51–S55), adding new data in Mozambique and Namibia reveals little new structure over Boyce and Cottaar (2021). Mean MTZ thickness in southern Africa is ~ 250 km compared to ~ 248 km previously. Results for Cameroon and Madagascar remain unchanged from Boyce and Cottaar (2021).

Increasing RF maximum frequency content (0.2–0.9 Hz) in CCP stacks shows the Turkana Depression is transitional between the Ethiopia-Yemen plateau and the East African plateau in mean d660 depth variability (~ 6 km, Figures S57–S58). The d660 below the East African plateau shows greater sensitivity to RF frequency (≤ 7 km mean d660 depth variability), while the Ethiopia-Yemen plateau displays less sensitivity (~ 4 km). d410 depths are broadly unchanged throughout East Africa as maximum frequency is increased. These results are independent of tomographic model chosen for depth correction.

4. Discussion

4.1. East Africa's Deep Mantle Upwellings—A New Plume Tail Below the Turkana Depression

AFRP22 illuminates distinct, slow velocity anomalies below the Ethiopia-Yemen and East African plateaus: A and B, respectively ($\delta V_p \leq -1.0\%$; Figures 4 and 5 and Figures S33–S39 in Supporting Information S1), that appear to extend continuously into the lower mantle ($> 2,000$ km depth). Anomaly B—the African Superplume—is a ubiquitous feature of most global and continental-scale models (e.g., Boyce et al., 2021; Chang et al., 2015, 2020; French & Romanowicz, 2014; Hansen et al., 2012; Li et al., 2008; Montelli et al., 2006; Ritsma et al., 1999; Simmons et al., 2012, see Figure S40 in Supporting Information S1). The upper mantle expression of anomaly A, often referred to as the Afar plume, has also been previously constrained seismologically and geochemically (Celli et al., 2020; Civiero et al., 2022; Debayle et al., 2001; Furman et al., 2006; Nelson et al., 2012; Rogers et al., 2000). However the vertical extent of anomaly A, throughout the entire mantle depth-range, has largely remained inconclusive because the majority of previous deep-penetrating tomographic models present limited evidence for a continuous upwelling rooted in the lower mantle (e.g., Chang & van der Lee, 2011; Chang et al., 2020; Hosseini et al., 2019; Montelli et al., 2006; Tsekhnistrenko et al., 2021, also see Figure S40 in Supporting Information S1). AFRP22 supports the conclusions of Boyce et al. (2021), who suggest that both anomalies A and B are likely instead whole mantle upwellings.

A striking new observation in Figures 4e, 4f, 5c–5f, and 5h is a narrow plume tail below SW Ethiopia/the NW Turkana Depression, persisting into the lower mantle: anomaly C ($\delta V_p \approx -0.4\%$). Anomaly C merges with anomaly A below southwestern Ethiopia around the base of the MTZ at 600–750 km depth (Figures 4 and 5; Figures S33–S35 in Supporting Information S1). Likely a product of our new seismograph station coverage in the Turkana Depression (Figure 2), this deep-seated plume tail has not been resolved before, though its existence has been inferred previously on the basis of upper mantle seismic images (e.g., Celli et al., 2020; Chang et al., 2020; Emry et al., 2019) and plate reconstructions (Vicente de Gouveia et al., 2018).

The apparent tilt of anomalies A and B (Figures 4 and 5) has also been observed previously to varying extents (e.g., Boyce et al., 2021; Hansen et al., 2012; Simmons et al., 2007; Tsekhnistrenko et al., 2021). However, AFRP22 shows little evidence for isolated upwellings within the African Superplume itself (anomaly B). Therefore support is lacking for the hypothesis of Davaille et al. (2005) and Tsekhnistrenko et al. (2021) that it is the result of the sequential release of multiple, vertically rising plumes. Furthermore, this hypothesis implies monotonically decreasing ages for East African magmatism moving south to north, for which no field-based evidence exists (e.g., George et al., 1998; Rooney et al., 2017). Our images of up to three completely distinct slow wavespeed anomalies, that persist from the base of the MTZ below East Africa to the CMB (anomalies A, B, C), agree with previous suggestions that more than one whole-mantle plume is required below the region (e.g., Boyce et al., 2021; George et al., 1998; Rogers et al., 2000). The improved apparent resolution offered by AFRP22 from upper-to-lower mantle depths below East Africa provides distinct advantages over existing P-wave models (e.g., Boyce et al., 2021; Hansen et al., 2012; Hosseini et al., 2019; Li et al., 2008; Montelli et al., 2006; Simmons et al., 2012, see Figure S40 in Supporting Information S1) and more shallowly penetrating S-wave counterparts (e.g., Celli et al., 2020; Chang & van der Lee, 2011) for both imaging the extent of deep mantle features and constraining their relation to tectonic processes. We return to this in Section 4.3.

4.2. Mantle Transition Zone Discontinuity Structure Across East Africa: Implications for Mantle Upwellings and Dynamic Topography

Receiver function CCP stacking results in Figure 7 reveal transition zone thinning below Afar and the Main Ethiopian Rift (10–15 km), consistent with the view that mantle temperatures are elevated at this depth range (e.g., Cornwell et al., 2011). Assuming average values for the d410 Clapeyron slope of $\delta P/\delta T_{d410} = 3.0 \text{ MPa/K}$ (Bina & Helffrich, 1994) and of $\delta P/\delta T_{d660} = -2.5 \text{ MPa/K}$ for the d660 Clapeyron slope (Ye et al., 2014) within the olivine transition yields a temperature anomaly of $\sim 100 \text{ K}$, if the temperature anomaly is zero where MTZ thickness is 250 km. Our results therefore contrast with those of Nyblade et al. (2000) and Thompson et al. (2015), who suggested a MTZ thermal anomaly below Ethiopia was largely lacking. Our observation of a thinned, and thus elevated temperature MTZ below the East African plateau, particularly the Eastern Rift (>10 km), also corroborates previous RF results (Mulib & Nyblade, 2013; Owens et al., 2000; Sun et al., 2017). The apparent variation in frequency dependence of the d660 depth between the Ethiopia-Yemen and East African plateaus (Figures S57–S58 in Supporting Information S1), helps corroborate previous work that suggests the Ethiopia-Yemen plateau overlies a moderate thermal upwelling, but that below the East African plateau overlies a stronger, thermochemical anomaly at MTZ depths (e.g., Boyce & Cottaar, 2021; Cornwell et al., 2011; Huerta et al., 2009).

A striking observation in Figure 7 is the markedly thin MTZ below southwest Ethiopia and the northwest Turkana Depression ($\leq 25 \text{ km}$), approximately coincident with anomaly C in the lower mantle of AFRP22 (Section 4.1; Figures 4 and 5). An apparent 4–6 km difference in d660 depth observed in this region, when varying RF maximum frequency (Figures S57–S58 in Supporting Information S1), suggests that the lower MTZ more closely resembles that below the East African plateau than the Ethiopia-Yemen plateau. This may point toward a southerly deep mantle origin associated with the African Superplume.

Concurrent analysis of AFRP22 and new MTZ thickness constraints allow us to reassess how mantle upwellings traverse the transition zone and impinge on the base of the overlying lithosphere. In contrast to Civiero et al. (2015), we find little evidence for multiple, distinct upwellings in the upper mantle ($< 660 \text{ km}$ depth). However, we cannot preclude the possibility that our lateral resolution is insufficient to resolve fine-scale heterogeneity (Figure S21 in Supporting Information S1). Instead, the observation that the sub-lithospheric upper mantle below both the Ethiopian and East African plateaus is ubiquitously seismically slow ($\delta V_p \leq -0.5\%$; Figures 4–6), corroborates the hypothesis that their high elevations are largely the result of dynamic mantle upwelling (e.g., Pik et al., 2008; Rogers et al., 2000). A slight reduction in uppermost-mantle slow wavespeed anomaly amplitudes is imaged around $\sim 5^\circ \text{N}$, $\sim 36^\circ \text{E}$ (Figure 6). This can likely be explained by a reduction in melt volumes associated with rifting in both the southern Main Ethiopian Rift (Ogden et al., 2021) and the Turkana Depression (Kounoudis et al., 2021) compared to the magma-rich central and northern Main Ethiopian Rift sectors to the north (e.g., Bastow et al., 2005, 2010; Kendall et al., 2005). Thus, we agree with the conclusions of Kounoudis et al. (2021) that there is no evidence for a break in dynamic mantle support below the Turkana Depression. Recent crustal RF analysis of the Turkana Depression crust (Ogden et al., 2023), and associated isostatic mass balance calculations (assuming Airy isostasy) are also consistent with this hypothesis. Ogden et al. (2023) reveal that Moho depths of 20–30 km across the Depression explain the region's low-lying nature compared to the adjacent plateaus to the north and south, with 550–645 m of mantle dynamic support required below the Depression.

4.3. Implications for Rifting and Cenozoic Flood Basalt Magmatism

Ethiopia is a unique laboratory for the investigation of rifting and hotspot tectonism because it offers the opportunity to study the thermo-mechanical state of the mantle responsible for it. However, although magmatism is ongoing in Ethiopia, the main phase of flood basaltic magmatism that capped the uplifted Ethiopia-Yemen plateau, occurred $\sim 30 \text{ Ma}$ (e.g., George et al., 1998; Rogers et al., 2000; Rooney, 2017). The African plate has subsequently drifted northward by ~ 500 – $1,000 \text{ km}$, meaning mantle directly underlying Ethiopia and Afar today is unlikely to be primarily responsible for the most voluminous flood basalt magmatism there (e.g., Ebinger & Sleep, 1998; Vicente de Gouveia et al., 2018). Therefore, to appreciate better the significance of our mantle tomographic and mantle transition zone results, we reconstruct African Plate motion in the Paleomagnetic reference frame following Müller et al. (2018) and Merdith et al. (2020). Figure 8 shows the present-day outline of flood basalt magmatism in Ethiopia would have overlain the thinnest patches of mantle transition zone at 30 Ma: below present day southwest Ethiopia/the northwest Turkana Depression, and northeastern Uganda/northwestern Kenya. Similarly, the northern tip of the flood basalt province was underlain by anomaly C in AFRP22 at $\sim 30 \text{ Ma}$.

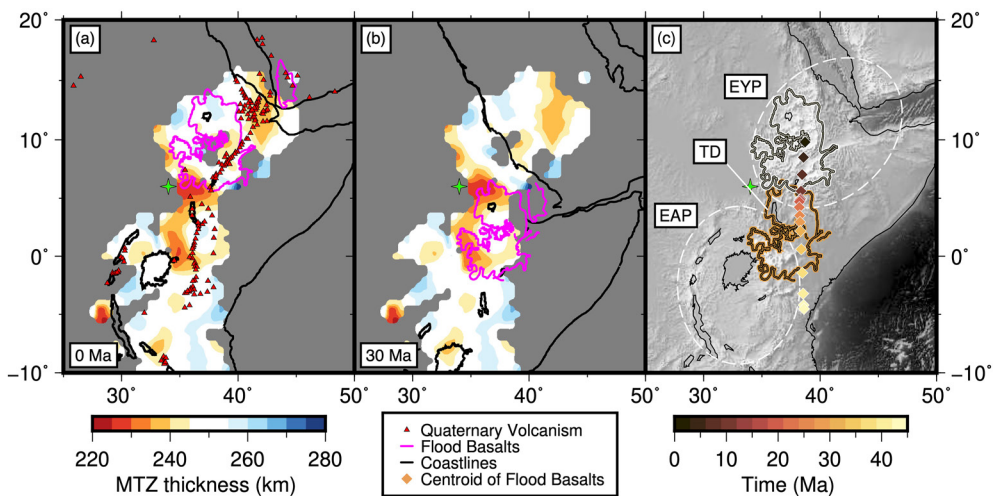


Figure 8. MTZ thickness (as per Figure 7) in present-day (a) and 30 Ma (b) plate configurations. Black lines: coastlines. (c) Centroid position of Ethiopia-Yemen flood basalt province since 45 Ma (diamonds) plotted over East African topography. The present day footprint of the Ethiopia-Yemen flood basalt province (white lines) is reconstructed to 30 Ma (orange). EYP: Ethiopia-Yemen plateau, EAP: East African plateau, TD: Turkana Depression. Plate motions reconstructed following Müller et al. (2018) and Merdith et al. (2020) using the Paleomagnetic reference frame. Green star: location of third East African plume proposed by Vicente de Gouveia et al. (2018).

(Figures 7 and 8). This assumes a stationary sub-plate mantle, and dominantly vertical flows in the upper mantle (e.g., Lawrence & Shearer, 2008). The colocation of flood basalts and thinned MTZ is likely robust in latitude. For example, this result is unchanged when a fixed Eurasian Plate is assumed in our reconstructions. However, longitudinal uncertainties, which affect reconstructions that rely on geomagnetic data, can account for some apparent lateral offset of the thinned MTZ and center of the flood basalts in our reconstructions (see Civiero et al., 2022, Figure S11 in Supporting Information S1 for Afar plume example).

Intriguingly, plotting the centroid of the flood basalt province since 45 Ma (Figure 8c), demonstrates that Africa's northward motion slowed at ~30 Ma, contemporaneous with the Eurasian-African collision and the development of Red Sea rifting (e.g., Jolivet & Faccenna, 2000). To some level, our results corroborate the hypothesis of Ebinger and Sleep (1998), who suggested that a plume was centered at ~8°N, 36°E at 45 Ma. Similarly, Vicente de Gouveia et al. (2018) proposed a plume centered at ~6°N, 34°E (Figures 4 and 8). Both of these putative plume locations are remarkably close to deep-seated anomaly C in AFRP22 (Figures 4 and 5) and substantially thinned MTZ in the NW Turkana Depression (Figures 7 and 8).

On the one hand, the observation that Ethiopia's flood basaltic magmatism developed during a period when the African plate stalled atop the hottest part of the mantle provides a compelling causative link between anomaly C and 30 Ma flood basalt magmatism. However, petrological analysis of Cenozoic basalts by Rooney et al. (2012) reveals only a slight reduction in mantle potential temperature anomaly between 30 Ma (~+170°C) and <10 Ma (~+140°C). The composition of Cenozoic hotspot and rifting-related magmatism also yields no evidence for plume heterogeneity throughout East Africa (Rooney, 2017), meaning the differential contributions to the upper mantle from AFRP22 anomalies A, B and C are indistinguishable in the geological record. A hypothesis of a well-mixed upper mantle, with lateral flow of plume material below lithospheric thin spots (e.g., Ebinger & Sleep, 1998) seems a likely scenario for East Africa.

At 100 km depth in AFRP22 (Figure 6), we do not image the narrow (50 km-wide), NW–SE-trending, fast wavespeed band shown by Kounoudis et al. (2021) to cross the southern extent of the Main Ethiopian Rift. Figure 3b shows this feature is below the resolving power of our tomographic inversion scheme, though slow wavespeed anomaly amplitudes are slightly reduced here ($\delta V_p = -0.3\%$ compared to $\delta V_p < -0.8\%$ 150 km to the north and south). However, below the southeasternmost Ethiopian plateau, AFRP22 provides the first evidence for fast wavespeed structure ($\delta V_p \approx 0.8\%$), consistent with refractory lithosphere that has resisted thermal and mechanical erosion during Cenozoic hotspot tectonism and rifting. Accordingly, flood basalt outcrops are absent atop this lithospheric block, which is likely at least Mesoproterozoic in age (e.g., Bianchini et al., 2014; Reisberg

et al., 2004; Stern et al., 2012). The southern edge of the SW-Ethiopian plateau fast wavespeed anomaly also marks the northern limit of failed, Mesozoic-age Anza rifting (Figure 6). Mesozoic rifting in Turkana is thus likely to have localized between two refractory Archean/Proterozoic lithospheric fragments—the Tanzanian Craton and southern Ethiopian Shield. We postulate that the mantle lithosphere of the southeastern Ethiopian Shield is likely more similar in composition/nature to the Tanzanian craton to the west, than to its northwestern Ethiopian plateau counterpart, which has witnessed substantial thermomechanical erosion in Cenozoic-to-recent times.

A final observation to draw from Figure 6 is the lack of slow wavespeed anomalies associated with the western rift, except around the Quaternary volcanoes of the Kivu and Virunga Volcanic Provinces. We find no evidence for linkage of the western rift with either the eastern or Main Ethiopian Rifts at upper mantle depths, in contrast to previous suggestions (e.g., Chorowicz, 2005). Thus, the boundary between the Nubian and Somalian plates at mantle lithospheric depths is confined to the eastern side of the Tanzanian craton.

5. Conclusions

Utilizing data from new seismograph networks in the Turkana Depression and northern Uganda we have constructed a new absolute P-wave whole-mantle tomographic model for Africa (AFRP22) and a P-to-s RF study of the African mantle transition zone. Our study is the first to analyze whole mantle structure using data from seismograph stations between, and atop, the Ethiopia-Yemen and East African plateaus.

Receiver functions show that the thinnest transition zone in East Africa is below the NW Turkana Depression and northern Uganda. AFRP22 reveals a previously unrecognized, approximately co-located, slow wavespeed plume tail, extending from the base of the mantle transition zone, deep into the lower mantle. Plate re-constructions demonstrate that the Ethiopia-Yemen flood basalt province lay above this plume tail and thinned MTZ, during its most voluminous eruption phase at 30 Ma. This present-day plume tail may thus have contributed, along with the lower mantle African Superplume, to the development of the flood basalt province.

A previously un-recognized zone of fast-wavespeed lithosphere below the southeastern-most Ethiopian plateau is interpreted as a refractory block of lithosphere on account of the lack of Cenozoic flood basalts there, and the observation that it marks the northern limited of failed Mesozoic Anza rifting.

Data Availability Statement

The facilities of IRIS Data Services, and specifically the IRIS Data Management Center, were used for access to waveforms, related metadata, and/or derived products used in this study. IRIS Data Services are funded through the Seismological Facilities for the Advancement of Geoscience (SAGE) Award of the National Science Foundation under Cooperative Support Agreement EAR-1851048. The seismic instruments were provided by the Incorporated Research Institutions for Seismology (IRIS) through the PASSCAL Instrument Center at New Mexico Tech. Data collected will be available through the IRIS Data Management Center. Phase arrivals from the EHB Bulletin are available at <http://www.isc.ac.uk/ehbbulletin/>. Seismic data was obtained (last accessed 08 Jan 2021) from the IRIS (<https://ds.iris.edu/ds/nodes/dmc/>) database. The waveform data used in this study, added to the data sets of Boyce et al. (2021) and Boyce and Cottaar (2021), are from the following networks: 6H-2011 (Fonseca et al., 2014; Helffrich & Fonseca, 2011), 8A-2015 (Durrheim & Nyblade, 2009; Nyblade, 2015), 9A-2019 (Bastow, 2019; Kounoudis et al., 2021), XW-2017 (Andriampanomanana et al., 2021; Nyblade, 2017), Y1-2018 (Ebinger, 2018; Kounoudis et al., 2021). Data was subsequently processed using IRIS products, Obspy (Beyreuther et al., 2010), ObspyDMT (Hosseini & Sigloch, 2017), SMURFPy (Seismological Methods Utilizing RFs in Python3 available at <https://doi.org/10.5281/zenodo.4337258>) and AARM (available as an electronic supplement in Boyce et al., 2017). A digital model file of AFRP22 is available at <https://doi.org/10.17611/dp/emc.2023.afnp22.1>. MTZ thickness values obtained in this study (Figure 7) are available as a Supplementary Text file that accompanies this manuscript (*Boyce_et_al_Africa_RFs_MTZ_thickness.txt*). Figures were plotted using matplotlib (<https://matplotlib.org/3.1.1/index.html>) and the Generic Mapping Tools (<https://www.generic-mapping-tools.org/>). The raw data files, processed data, inversion software package and plotting codes (Boyce, 2023) will be available, following lifting of data embargo, on 2024-05-24 at <https://doi.org/10.5281/zenodo.7607098>.

Acknowledgments

This project received funding from the Natural Environment Research Council [NERC grant reference number NE/R010862/1] and the European Research Council (ERC) under the European Union's Horizon 2020 research and innovation program (grant agreement No. 804071 -ZoomDeep), both awarded to S.Cottaar. I. D. Bastow acknowledges support from Natural Environment Research Council Grant NE/S014136/1. C. J. Ebinger acknowledges National Science Foundation NSF-GEO-NERC award 1824417. We thank the editor and three reviewers for thoughtful comments that helped clarify the manuscript novelty. A.B./I.D.B./S.C Designed the study, A.B./R.K./C.S.O conducted data processing, A.B. conducted tomographic inversion and RF imaging, A.B./I.D.B./R.K./C.S.C./C.J.E interpreted data, A.B. prepared initial manuscript. All authors revised/drafted manuscript critically and approved final version.

References

- Andriamponomanana, F., Nyblade, A. A., Durrheim, R., Tugume, F., & Nyago, J. (2021). Shear wave splitting measurements in northeastern Uganda and southeastern Tanzania: Corroborating evidence for sublithospheric mantle flow beneath East Africa. [Dataset]. *Geophysical Journal International*, 226, 1696–1704. <https://doi.org/10.1093/gji/ggab167>
- Bastow, I. D. (2012). Relative arrival-time upper-mantle tomography and the elusive background mean. *Geophysical Journal International*, 190(2), 1271–1278. <https://doi.org/10.1111/j.1365-246X.2012.05559.x>
- Bastow, I. D. (2019). Turkana rift arrays to investigate lithospheric strains (TRAILS)—UK component [Dataset]. International Federation of Digital Seismograph Networks. (Seismic Network). https://doi.org/10.7914/SN/9A_2019
- Bastow, I. D., Pilidou, S., Kendall, J.-M., & Stuart, G. (2010). Melt-induced seismic anisotropy and magma assisted rifting in Ethiopia: Evidence from surface waves. *Geochemistry, Geophysics, Geosystems*, 11(6). <https://doi.org/10.1029/2010GC003036>
- Bastow, I. D., Stuart, G., Kendall, J.-M., & Ebinger, C. J. (2005). Upper-mantle seismic structure in a region of incipient continental breakup: Northern Ethiopian rift. *Geophysical Journal International*, 162(2), 479–493. <https://doi.org/10.1111/j.1365-246X.2005.02666.x>
- Begg, G. C., Griffin, W. L., Natapov, L. M., O'Reilly, S. Y., Grand, S. P., O'Neill, C. J., et al. (2009). The lithospheric architecture of Africa: Seismic tomography, mantle petrology, and tectonic evolution. *Geosphere*, 5(1), 23–50. <https://doi.org/10.1130/GES00179.1>
- Benoit, M. H., Nyblade, A. A., Owens, T. J., & Stuart, G. (2006). Mantle transition zone structure and upper mantle S velocity variations beneath Ethiopia: Evidence for a broad, deep-seated thermal anomaly. *Geochemistry, Geophysics, Geosystems*, 7(11), Q11013. <https://doi.org/10.1029/2006GC001398>
- Benoit, M. H., Nyblade, A. A., & Paschos, M. E. (2006). Crustal thinning between the Ethiopian and East African Plateaus from modeling Rayleigh wave dispersion. *Geophysical Research Letters*, 33(13), L13301. <https://doi.org/10.1029/2006GL025687>
- Beyreuther, M., Barsch, R., Krischer, L., Megies, T., Behr, Y., & Wassermann, J. (2010). ObsPy: A python toolbox for seismology. [Software]. *Seismological Research Letters*, 81, 530–533. <https://doi.org/10.1785/gssrl.81.3.530>
- Bianchini, G., Bryce, J. G., Blachert-Toft, J., Beccaluva, L., & Natali, C. (2014). Mantle dynamics and secular variations beneath the East African Rift: Insights from peridotite xenoliths (Mega, Ethiopia). *Chemical Geology*, 386, 49–58. <https://doi.org/10.1016/j.chemgeo.2014.07.024>
- Bina, C. R., & Helffrich, G. R. (1994). Phase transition Clapeyron slopes and transition zone seismic discontinuity topography. *Journal of Geophysical Research*, 99(B8), 15853. <https://doi.org/10.1029/94jb00462>
- Boyce, A. (2023). AFRP22 tomographic model & MTZ receiver functions: Data, software, plotting (1.0). [Dataset]. Zenodo. <https://doi.org/10.5281/zenodo.7607098>
- Boyce, A., Bastow, I. D., Cottaar, S., Kounoudis, R., Guilloud De Courbeville, J., Caunt, E., & Desai, S. (2021). AFRP20: New P-wavespeed model for the african mantle reveals two whole-mantle plumes below East Africa and Neoproterozoic Modification of the Tanzania Craton. *Geochemistry, Geophysics, Geosystems*, 22(3). <https://doi.org/10.1029/2020GC009302>
- Boyce, A., Bastow, I. D., Rondenay, S., & Van der Hilst, R. D. (2017). From relative to absolute teleseismic travel-times: The absolute arrival-time recovery method (AARM) [Software]. *Bulletin of the Seismological Society of America*, 107, 2511–2520. <https://doi.org/10.1785/0120170021>
- Boyce, A., & Cottaar, S. (2021). Insights into deep mantle thermochemical contributions to African magmatism from converted seismic phases. *Geochemistry, Geophysics, Geosystems*, 22(3). <https://doi.org/10.1029/2020GC009478>
- Braile, L., Wang, B., Daudt, C., Keller, G., & Patel, J. P. (1994). Modeling the 2-D seismic velocity structure across the Kenya rift. *Tectonophysics*, 236(1–4), 251–269. [https://doi.org/10.1016/0040-1951\(94\)90179-1](https://doi.org/10.1016/0040-1951(94)90179-1)
- Brown, F. H., & McDougall, I. (2011). Geochronology of the Turkana Depression of northern Kenya and southern Ethiopia. *Evolutionary Anthropology*, 20(6), 217–227. <https://doi.org/10.1002/evan.20318>
- Celli, N. L., Lebedev, S., Schaeffer, A. J., & Gaina, C. (2020). African cratonic lithosphere carved by mantle plumes. *Nature Communications*, 11(1), 92. <https://doi.org/10.1038/s41467-019-13871-2>
- Chang, S. J., Ferreira, A. M. G., Ritsema, J., Van Heijst, H.-J., & Woodhouse, J. H. (2015). Joint inversion for global isotropic and radially anisotropic mantle structure including crustal thickness perturbations. *Journal of Geophysical Research*, 120(6), 4278–4300. <https://doi.org/10.1002/2014jb011824>
- Chang, S. J., Kendall, E., Davaille, A., & Ferreira, A. M. G. (2020). The evolution of mantle plumes in East Africa. *Journal of Geophysical Research*, 125(12). <https://doi.org/10.1029/2020jb019929>
- Chang, S. J., & van der Lee, S. (2011). Mantle plumes and associated flow beneath Arabia and East Africa. *Earth and Planetary Science Letters*, 302(3–4), 448–454. <https://doi.org/10.1016/j.epsl.2010.12.050>
- Chorowicz, J. (2005). The East African rift system. *Journal of African Earth Sciences*, 43(1–3), 379–410. <https://doi.org/10.1016/j.jafarsci.2005.07.019>
- Civiero, C., Armitage, J. J., Goes, S., & Hammond, J. O. S. (2019). The seismic signature of upper-mantle plumes: Application to the northern East African rift. *Geochemistry, Geophysics, Geosystems*, 20(12), 6106–6122. <https://doi.org/10.1029/2019gc008636>
- Civiero, C., Goes, S., Hammond, J. O. S., Fishwick, S., Ahmed, A., Ayele, A., et al. (2016). Small-scale thermal upwellings under the northern East African Rift from S travel time tomography. *Journal of Geophysical Research*, 121(10), 7395–7408. <https://doi.org/10.1002/2016JB013070>
- Civiero, C., Hammond, J. O. S., Goes, S., Fishwick, S., Ahmed, A., Ayele, A., et al. (2015). Multiple mantle upwellings in the transition zone beneath the northern East-African Rift system from relative P-wave travel-time tomography. *Geochemistry, Geophysics, Geosystems*, 16(9), 2949–2968. <https://doi.org/10.1002/2015GC005948>
- Civiero, C., Lebedev, S., & Celli, N. L. (2022). A complex mantle plume head below East Africa-Arabia shaped by the lithosphere-asthenosphere boundary topography. *Geochemistry, Geophysics, Geosystems*, 23(11), e2022GC010610. <https://doi.org/10.1029/2022gc010610>
- Cornwell, D., Hetényi, G., & Blanchard, T. (2011). Mantle transition zone variations beneath the Ethiopian Rift and Afar: Chemical heterogeneity within a hot mantle? *Geophysical Research Letters*, 38(16). <https://doi.org/10.1029/2011gl047575>
- Cottaar, S., Pugh, S., Boyce, A., & Jenkins, J. (2020). Smurphy: Seismological methods utilizing receiver functions in python3. [Software]. Zenodo. <https://doi.org/10.5281/zenodo.4337258>
- Davaille, A., Stutzmann, E., Silveira, G., Besse, J., & Courtillot, V. (2005). Convective patterns under the Indo-Atlantic box. *Earth and Planetary Science Letters*, 239(3–4), 233–252. <https://doi.org/10.1016/j.epsl.2005.07.024>
- Debayle, E., Lévéque, J., & Cara, M. (2001). Seismic evidence for a deeply rooted low-velocity anomaly in the upper mantle beneath the northeastern Afro/Arabian continent. *Earth and Planetary Science Letters*, 193(3–4), 423–436. [https://doi.org/10.1016/S0012-821X\(01\)00509-X](https://doi.org/10.1016/S0012-821X(01)00509-X)
- Dueker, K. G., & Sheehan, A. F. (1997). Mantle discontinuity structure from midpoint stacks of converted P to S waves across the Yellowstone hotspot track. *Journal of Geophysical Research*, 102(B4), 8313–8327. <https://doi.org/10.1029/96jb03857>
- Durrheim, R. J., Nyblade, A. A., & Dirks, P. H. G. M. (2009). Africa array special volume—Introduction [Dataset]. South African Journal of Geology, 112, 209–212. <https://doi.org/10.2113/gssajg.112.3-4.209>

- Ebinger, C. J. (2018). Crust and mantle structure and the expression of extension in the Turkana Depression of Kenya and Ethiopia [Dataset]. International Federation of Digital Seismograph Networks. (Seismic Network). https://doi.org/10.7914/SN/Y1_2018
- Ebinger, C. J., & Sleep, N. (1998). Cenozoic magmatism throughout East Africa resulting from impact of a single plume. *Nature*, 395(6704), 788–791. <https://doi.org/10.1038/27417>
- Ebinger, C. J., Yemane, T., Harding, D., Tesfaye, S., Kelley, S., & Rex, D. (2000). Rift deflection, migration, and propagation: Linkage of the Ethiopian and Eastern rifts, Africa. *Bulletin of the Seismological Society of America*, 91(2), 163–176. [https://doi.org/10.1130/0016-7606\(2000\)91<163:rdmapl>2.0.co;2](https://doi.org/10.1130/0016-7606(2000)91<163:rdmapl>2.0.co;2)
- Emry, E. L., Shen, Y., Nyblade, A. A., Flinders, A., & Bao, X. (2019). Upper mantle Earth structure in Africa from full-wave ambient noise tomography. *Geochemistry, Geophysics, Geosystems*, 20(1), 120–147. <https://doi.org/10.1029/2018gc007804>
- Engdahl, E. R., Van der Hilst, R. D., & Buland, R. (1998). Global teleseismic earthquake relocation with improved travel times and procedures for depth determination. *Bulletin of the Seismological Society of America*, 88(3), 722–743. <https://doi.org/10.1785/bssa0880030722>
- Fonseca, J. F. B. D., Chamussa, J., Domingues, A., Helffrich, G., Antunes, E., van Aswegen, G., et al. (2014). MOZART: A seismological investigation of the East African Rift in Central Mozambique [Dataset]. Seismological Research Letters, 85, 108–116. <https://doi.org/10.1785/0220130082>
- French, S. W., & Romanowicz, B. (2014). Whole-mantle radially anisotropic shear velocity structure from spectral-element waveform tomography. *Geophysical Journal International*, 199(3), 1303–1327. <https://doi.org/10.1093/gji/ggu334>
- Fritz, H., Abdelsalam, M., Ali, K. A., Bingen, B., Collins, A. S., Fowler, A. R., et al. (2013). Orogen styles in the East African Orogen: A review of the neoproterozoic to cambrian tectonic evolution. *Journal of African Earth Sciences*, 86, 65–106. <https://doi.org/10.1016/j.jafrearsci.2013.06.004>
- Furman, T., Bryce, J. G., Rooney, T. O., Hanan, B. B., Yirgu, G., & Ayalew, D. (2006). Heads and tails: 30 million years of the Afar plume. *Geological Society, London, Special Publications*, 259(1), 95–119. <https://doi.org/10.1144/GSL.SP.2006.259.01.09>
- Gallacher, R. J., Keir, D., Harmon, N., Stuart, G., Leroy, S., Hammond, J. O. S., et al. (2016). The initiation of segmented buoyancy-driven melting during continental breakup. *Nature Communications*, 7(1), 13110. <https://doi.org/10.1038/ncomms13110>
- George, R., Rogers, N. W., & Kelley, S. (1998). Earliest magmatism in Ethiopia: Evidence for two mantle plumes in one continental flood basalt province. *Geology*, 26(10), 923–926. [https://doi.org/10.1130/0091-7613\(1998\)026<923:EMIEEF>2.3.CO;2](https://doi.org/10.1130/0091-7613(1998)026<923:EMIEEF>2.3.CO;2)
- Hammond, W. C., & Humphreys, E. D. (2000). Upper mantle seismic wave velocity: Effects of realistic partial melt geometries. *Journal of Geophysical Research*, 105(B5), 10975–10986. <https://doi.org/10.1029/2000jb900041>
- Hansen, S. E., Nyblade, A. A., & Benoit, M. H. (2012). Mantle structure beneath Africa and Arabia from adaptively parameterized P-wave tomography: Implications for the origin of Cenozoic Afro-Arabian tectonism. *Earth and Planetary Science Letters*, 319, 23–34. <https://doi.org/10.1016/j.epsl.2011.12.023>
- Heit, B., Yuan, X., Weber, M., Geissler, W., Jokat, W., Lushetile, B., & Hoffmann, K. (2015). Crustal thickness and Vp/Vs ratio in NW Namibia from receiver functions: Evidence for magmatic underplating due to mantle plume-crust interaction. *Geophysical Research Letters*, 42(9), 3330–3337. <https://doi.org/10.1002/2015gl063704>
- Helffrich, G. R. (2000). Topography of the transition zone seismic discontinuities. *Review of Geophysics*, 38(1), 141–158. <https://doi.org/10.1029/1999RG000060>
- Helffrich, G. R., & Fonseca, J. F. B. D. (2011). Mozambique rift tomography [Dataset]. International Federation of Digital Seismograph Networks. (Seismic Network). https://doi.org/10.7914/SN/6H_2011
- Hosseini, K., & Sigloch, K. (2017). ObspyDMT: A Python toolbox for retrieving and processing large seismological data sets [Software]. *Solid Earth*, 8, 1047–1070. <https://doi.org/10.5194/se-8-1047-2017>
- Hosseini, K., Sigloch, K., Tsekhmistrov, M., Zaheri, A., Nissen-Meyer, T., & Igel, H. (2019). Global mantle structure from multifrequency tomography using P, PP and P-diffracted waves. *Geophysical Journal International*, 220(1), 96–141. <https://doi.org/10.1093/gji/ggz394>
- Huerta, A. D., Nyblade, A. A., & Reusch, A. M. (2009). Mantle transition zone structure beneath Kenya and Tanzania: More evidence for a deep-seated thermal upwelling in the mantle. *Geophysical Journal International*, 177(3), 1249–1255. <https://doi.org/10.1111/j.1365-246x.2009.04092.x>
- Jolivet, L., & Faccenna, C. (2000). Mediterranean extension and the Africa-Eurasia collision. *Tectonics*, 19(6), 1095–1106. <https://doi.org/10.1029/2000tc900018>
- Káráson, H., & Van der Hilst, R. D. (2001). Tomographic imaging of the lowermost mantle with differential times of refracted and diffracted core phases (PKP, P diff). *Journal of Geophysical Research*, 106(B4), 6569–6587. <https://doi.org/10.1029/2000jb900380>
- Kendall, J.-M., Stuart, G., Ebinger, C. J., Bastow, I. D., & Keir, D. (2005). Magma assisted rifting in Ethiopia. *Nature*, 433(7022), 146–148. <https://doi.org/10.1038/nature03161>
- Kennett, B. L. N., Engdahl, E. R., & Buland, R. (1995). Constraints on seismic velocities in the Earth from traveltimes. *Geophysical Journal International*, 122(1), 108–124. <https://doi.org/10.1111/j.1365-246X.1995.tb03540.x>
- Kennett, B. L. N., & Gudmundsson, O. (1996). Ellipticity corrections for seismic phases. *Geophysical Journal International*, 127(1), 40–48. <https://doi.org/10.1111/j.1365-246x.1996.tb01533.x>
- Kounoudis, R., Bastow, I. D., Ebinger, C. J., Ogden, C. S., Ayele, A., Bendick, R., et al. (2021). Body-wave tomographic imaging of the Turkana Depression: Implications for rift development and plume-lithosphere interactions [Dataset]. *Geochemistry, Geophysics, Geosystems*, 22. <https://doi.org/10.1029/2021gc009782>
- Laske, G., Masters, G., Ma, Z., & Pasquano, M. E. (2013). Update on CRUST1.0—A 1-degree global model of Earth's crust. *Geophysical Research Abstracts*, 15, abstract egu2013-2658 (p. EGU2013-2658).
- Lawrence, J. F., & Shearer, P. M. (2008). Imaging mantle transition zone thickness with SdS–SS finite-frequency sensitivity kernels. *Geophysical Journal International*, 174(1), 143–158. <https://doi.org/10.1111/j.1365-246x.2007.03673.x>
- Li, C., Van der Hilst, R. D., Engdahl, R., & Burdick, S. (2008). A new global model for P wave speed variations in Earth's mantle. *Geochemistry, Geophysics, Geosystems*, 9(5). <https://doi.org/10.1029/2007GC001806>
- Ligorria, J., & Ammon, C. (1999). Iterative deconvolution and receiver-function estimation. *Bulletin of the Seismological Society of America*, 89(5), 1395–1400. <https://doi.org/10.1785/bssa0890051395>
- Lu, C., Grand, S. P., Lai, H., & Garnero, E. J. (2019). TX2019slab: A new P and S tomography model incorporating subducting slabs. *Journal of Geophysical Research*, 124(11), 11549–11567. <https://doi.org/10.1029/2019jb017448>
- Macgregor, D. (2015). History of the development of the East African rift system: A series of interpreted maps through time. *Journal of African Earth Sciences*, 101, 232–252. <https://doi.org/10.1016/j.jafrearsci.2014.09.016>
- Mechie, J., Keller, G., Prodehl, C., Gaciri, S., Braile, L., Mooney, W., et al. (1994). Crustal structure beneath the Kenya Rift from axial profile data. *Tectonophysics*, 236(1–4), 179–200. [https://doi.org/10.1016/0040-1951\(94\)90176-7](https://doi.org/10.1016/0040-1951(94)90176-7)

- Merdith, A. S., Williams, S. E., Collins, A. S., Tetley, M. G., Mulder, J. A., Blades, M. L., et al. (2020). Extending full-plate tectonic models into deep time: Linking the Neoproterozoic and the Phanerozoic. *Earth-Science Reviews*, 214, 103477. <https://doi.org/10.1016/j.earscirev.2020.103477>
- Montagner, J. P., Marty, B., Stutzmann, E., Sicilia, D., Cara, M., Pik, R., et al. (2007). Mantle upwellings and convective instabilities revealed by seismic tomography and helium isotope geochemistry beneath eastern Africa. *Geophysical Research Letters*, 34(21), L21303. <https://doi.org/10.1029/2007gl031098>
- Montelli, R., Nolet, G., Dahlen, F., & Masters, G. (2006). A catalogue of deep mantle plumes: New results from finite-frequency tomography. *Geochemistry, Geophysics, Geosystems*, 7(11), Q11007. <https://doi.org/10.1029/2006GC001248>
- Morley, C., Wescott, W., Stone, D., Harper, R., Wigger, S., & Karanja, F. (1992). Tectonic evolution of the northern Kenyan Rift. *Journal of the Geological Society*, 149(3), 333–348. <https://doi.org/10.1144/gsjgs.149.3.0333>
- Mulibio, G. D., & Nyblade, A. A. (2013). Mantle transition zone thinning beneath eastern Africa: Evidence for a whole-mantle superplume structure. *Geophysical Research Letters*, 40(14), 3562–3566. <https://doi.org/10.1002/grl.50694>
- Müller, R. D., Cannon, J., Qin, X., Watson, R. J., Gurnis, M., Williams, S., et al. (2018). GPlates: Building a virtual Earth through deep time. *Geochemistry, Geophysics, Geosystems*, 19(7), 2243–2261. <https://doi.org/10.1029/2018gc007584>
- Nelson, W. R., Furman, T., van Keken, P. E., Shirey, S. B., & Hanan, B. B. (2012). Os/Hf isotopic insight into mantle plume dynamics beneath the East African Rift System. *Chemical Geology*, 320(189), 66–79. <https://doi.org/10.1016/j.chemgeo.2012.05.020>
- Nyblade, A. A. (2015). AfricaArray—Namibia [Dataset]. IRIS. (Seismic Network). https://doi.org/10.7914/SN/A8_A_2015
- Nyblade, A. A. (2017). Broadband seismic experiment in NE Uganda to investigate plume-lithosphere interactions [Dataset]. International Federation of Digital Seismograph Networks. (Seismic Network). https://doi.org/10.7914/SNXW_2017
- Nyblade, A. A., Knox, R., & Gurrola, H. (2000). Mantle transition zone thickness beneath Afar: Implications for the origin of the Afar hotspot. *Geophysical Journal International*, 142(2), 615–619. <https://doi.org/10.1046/j.1365-246x.2000.00179.x>
- Ogden, C. S., Bastow, I. D., Ebinger, C. J., Ayele, A., Kounoudis, R., Musila, M., et al. (2023). The development of multiple phases of superposed rifting in the Turkana Depression, East Africa: Evidence from receiver functions. *Earth and Planetary Science Letters*, 609, 118088. <https://doi.org/10.1016/j.epsl.2023.118088>
- Ogden, C. S., Keir, D., Bastow, I. D., Ayele, A., Marcou, S., Ugo, F., et al. (2021). Seismicity and crustal structure of the southern main Ethiopian rift: New evidence from Lake Abaya. *Geochemistry, Geophysics, Geosystems*, 22(8). <https://doi.org/10.1029/2021gc009831>
- Owens, T. J., Nyblade, A. A., Gurrola, H., & Langston, C. A. (2000). Mantle transition zone structure beneath Tanzania, east Africa. *Geophysical Research Letters*, 27(6), 827–830. <https://doi.org/10.1029/1999gl005429>
- Pik, R., Marty, B., Carignan, J., & Lavé, J. (2003). Stability of the Upper Nile drainage network (Ethiopia) deduced from (U–Th)/He thermochronometry: Implications for uplift and erosion of the Afar plume dome. *Earth and Planetary Science Letters*, 215(1–2), 73–88. [https://doi.org/10.1016/s0012-821x\(03\)00457-6](https://doi.org/10.1016/s0012-821x(03)00457-6)
- Pik, R., Marty, B., Carignan, J., Yirgu, G., & Ayalew, T. (2008). Timing of East African Rift development in southern Ethiopia: Implication for mantle plume activity and evolution of topography. *Geology*, 36(2), 167–170. <https://doi.org/10.1130/g24233a.1>
- Prodehl, C., Jacob, A., Thybo, H., Dindi, E., & Stangl, R. (1994). Crustal structure on the northeastern flank of the Kenya rift. *Tectonophysics*, 236(1–4), 271–290. [https://doi.org/10.1016/0040-1951\(94\)90180-5](https://doi.org/10.1016/0040-1951(94)90180-5)
- Pugh, S., Boyce, A., Bastow, I. D., Ebinger, C. J., & Cottaar, S. (2023). Multigenetic origin of the X-discontinuity below continents: Insights from African receiver functions. *Geochemistry, Geophysics, Geosystems*, 24(3). <https://doi.org/10.1029/2022gc010782>
- Purcell, P. G. (2018). Re-Imagining and re-imaging the development of the East African Rift. *Petroleum Geology*, 24(1), 21–40. <https://doi.org/10.1144/petgeo2017-036>
- Reed, C. A., Gao, S. S., Liu, K. H., & Yu, Y. (2016). The mantle transition zone beneath the Afar depression and adjacent regions: Implications for mantle plumes and hydration. *Geophysical Journal International*, 205(3), 1756–1766. <https://doi.org/10.1093/gji/ggw116>
- Reisberg, L., Lorand, J.-P., & Bedini, R. (2004). Reliability of Os model ages in pervasively metasomatized continental mantle lithosphere: A case study of sidamo spinel peridotite xenoliths (East African rift, Ethiopia). *Chemical Geology*, 208(1–4), 119–140. <https://doi.org/10.1016/j.chemgeo.2004.04.008>
- Ritsema, J., Deuss, A., Van Heijst, H.-J., & Woodhouse, J. (2011). S40RTS: A degree-40 shear-velocity model for the mantle from new Rayleigh wave dispersion, teleseismic traveltimes and normal-mode splitting function measurements. *Geophysical Journal International*, 184(3), 1223–1236. <https://doi.org/10.1111/j.1365-246X.2010.04884.x>
- Ritsema, J., Nyblade, A. A., Owens, T. J., Langston, C., & VanDecar, J. (1998). Upper mantle seismic velocity structure beneath Tanzania, East Africa: Implications for the stability of cratonic lithosphere. *Journal of Geophysical Research*, 103(B9), 21201–21213. <https://doi.org/10.1029/98JB01274>
- Ritsema, J., & Van Heijst, H.-J. (2002). Constraints on the correlation of P- and S-wave velocity heterogeneity in the mantle from P, PP, PPP and PKPab traveltimes. *Geophysical Journal International*, 149(2), 482–489. <https://doi.org/10.1046/j.1365-246x.2002.01631.x>
- Ritsema, J., Van Heijst, H.-J., & Woodhouse, J. (1999). Complex shear wave velocity structure imaged beneath Africa and Iceland. *Science*, 286(5446), 1925–1928. <https://doi.org/10.1126/science.286.5446.1925>
- Rogers, N. W., Macdonald, R., Fitton, J., George, R., Smith, R., & Barreiro, B. (2000). Two mantle plumes beneath the East African rift system: Sr, Nd and Pb isotope evidence from Kenya rift basalts. *Earth and Planetary Science Letters*, 176(3–4), 387–400. [https://doi.org/10.1016/s0012-821x\(00\)00012-1](https://doi.org/10.1016/s0012-821x(00)00012-1)
- Rooney, T. O. (2017). The cenozoic magmatism of East-Africa: Part I — Flood basalts and pulsed magmatism. *Lithos*, 286–287, 264–301. <https://doi.org/10.1016/j.lithos.2017.05.014>
- Rooney, T. O., Furman, T., Yirgu, G., & Ayalew, D. (2005). Structure of the Ethiopian lithosphere: Xenolith evidence in the main Ethiopian rift. *Geochimica et Cosmochimica Acta*, 69(15), 3889–3910. <https://doi.org/10.1016/j.gca.2005.03.043>
- Rooney, T. O., Herzberg, C., & Bastow, I. D. (2012). Elevated mantle temperature beneath East Africa. *Geology*, 40(G32382R1), 27–40. <https://doi.org/10.1130/G32382.1>
- Rooney, T. O., Lavigne, A., Svoboda, C., Girard, G., Yirgu, G., Ayalew, D., & Kappelman, J. (2017). The making of an underplate: Pyroxenites from the Ethiopian lithosphere. *Chemical Geology*, 455, 264–281. <https://doi.org/10.1016/j.chemgeo.2016.09.011>
- Schaeffer, A., & Lebedev, S. (2013). Global shear speed structure of the upper mantle and transition zone. *Geophysical Journal International*, 194(1), 417–449. <https://doi.org/10.1093/gji/ggt095>
- Simmons, N. A., Forte, A. M., & Grand, S. P. (2007). Thermochemical structure and dynamics of the African superplume. *Geophysical Research Letters*, 34(2), L02301. <https://doi.org/10.1029/2006GL028009>
- Simmons, N. A., Myers, S. C., Johannesson, G., & Matzel, E. (2012). LLNL-G3Dv3: Global P wave tomography model for improved regional and teleseismic travel time prediction. *Journal of Geophysical Research*, 117(B10). <https://doi.org/10.1029/2012jb009525>

- Stern, R. J., Ali, K. A., Abdelsalam, M. G., Wilde, S. A., & Zhou, Q. (2012). U–Pb zircon geochronology of the eastern part of the Southern Ethiopian Shield. *Precambrian Research*, 206, 159–167. <https://doi.org/10.1016/j.precamres.2012.02.008>
- Sun, M., Liu, K. H., Fu, X., & Gao, S. S. (2017). Receiver function imaging of mantle transition zone discontinuities beneath the Tanzania craton and Adjacent segments of the East African Rift system. *Geophysical Research Letters*, 44(24), 12116–12124. <https://doi.org/10.1002/2017gl075485>
- Tesoniero, A., Cammarano, F., & Boschi, L. (2016). S-to-P heterogeneity ratio in the lower mantle and thermo-chemical implications. *Geochemistry, Geophysics, Geosystems*, 17(7), 2522–2538. <https://doi.org/10.1002/2016gc006293>
- Thompson, D. A., Hammond, J. O. S., Kendall, J., Stuart, G. W., Helffrich, G. R., Keir, D., et al. (2015). Hydrous upwelling across the mantle transition zone beneath the Afar Triple Junction. *Geochemistry, Geophysics, Geosystems*, 16(3), 834–846. <https://doi.org/10.1002/2014gc005648>
- Tsekhnistrenko, M., Sigloch, K., Hosseini, K., & Barruol, G. (2021). A tree of Indo-African mantle plumes imaged by seismic tomography. *Nature Geoscience*, 14, 1–8. <https://doi.org/10.1038/s41561-021-00762-9>
- VanDecar, J., & Crosson, R. (1990). Determination of teleseismic relative phase arrival times using multi-channel cross-correlation and least squares. *Bulletin of the Seismological Society of America*, 80(1), 150–169.
- van Stiphout, A. M., Cottaar, S., & Deuss, A. (2019). Receiver function mapping of mantle transition zone discontinuities beneath Alaska using scaled 3-D velocity corrections. *Geophysical Journal International*, 219(2), 1432–1446. <https://doi.org/10.1093/gji/ggz360>
- Vicente de Gouveia, S., Besse, J., Frizon de Lamotte, D., Greff-Lefftz, M., Lescanne, M., Gueydan, F., & Leparnier, F. (2018). Evidence of hotspot paths below Arabia and the Horn of Africa and consequences on the Red Sea opening. *Earth and Planetary Science Letters*, 487, 210–220. <https://doi.org/10.1016/j.epsl.2018.01.030>
- Ye, Y., Gu, C., Shim, S.-H., Meng, Y., & Prakapenka, V. (2014). The postspinel boundary in pyrolytic compositions determined in the laser-heated diamond anvil cell. *Geophysical Research Letters*, 41(11), 3833–3841. <https://doi.org/10.1002/2014gl060060>